VULCAN

Reflectivity Measurements on DUNE Samples in the VUV Range

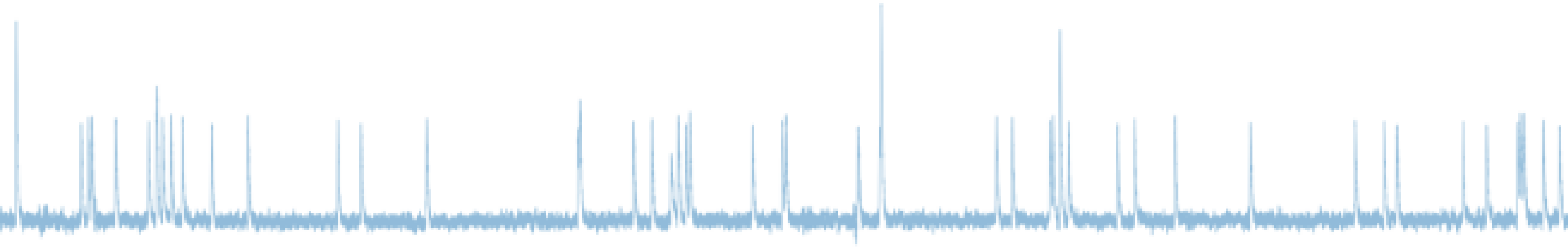

Master thesis Corryenne Groen

Supervisor: dr. T.R. Pollmann
Daily supervisor 1: M. van Nuland-Troost
Daily supervisor 2: V. Gupta
Second examiner: prof. dr. P.J. de Jong

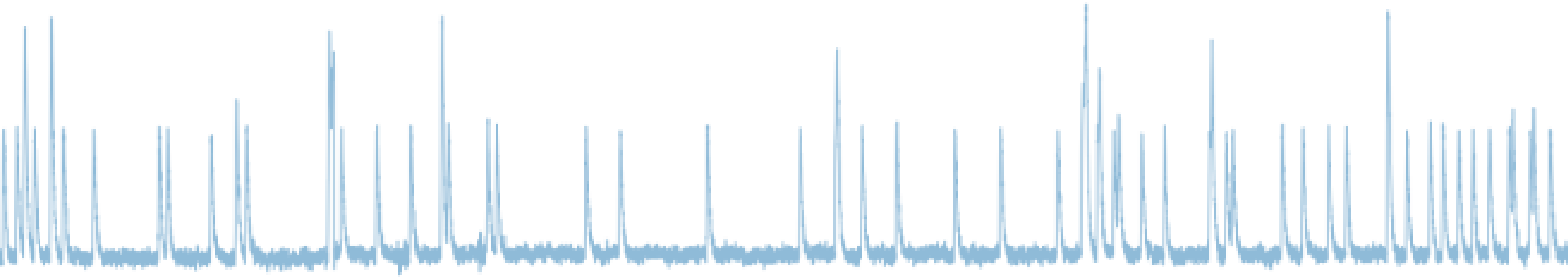

October 17, 2024

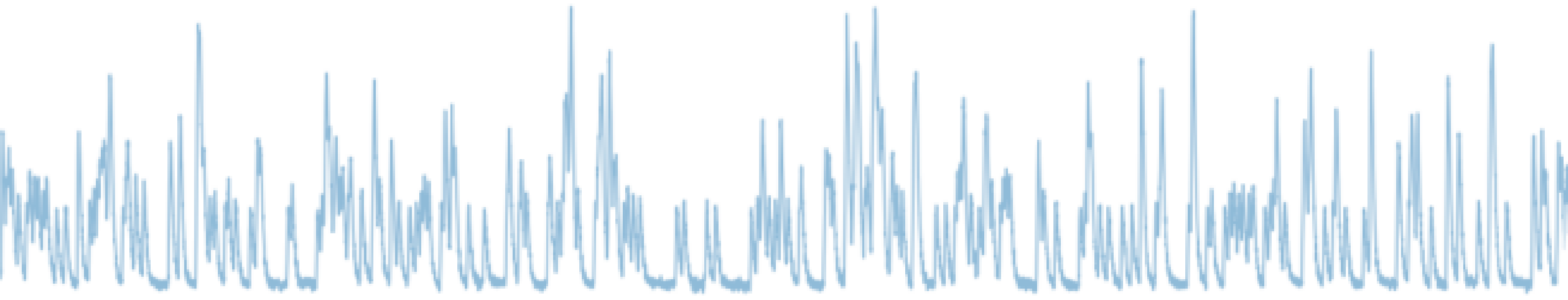

Abstract

Neutrinos are among the most intriguing particles in the universe. Despite their abundance, their extremely small mass and weak interactions make them incredibly difficult to detect. A deeper understanding of neutrinos could provide crucial insights into the fundamental nature of particle physics. One of the most ambitious attempts to detect and study neutrinos is the Deep Underground Neutrino Experiment (DUNE). DUNE makes use of a time projection chamber (TPC) filled with liquid argon (LAr) as a detection medium. It will capture charged particles generated by neutrino interactions. Additionally, the detector will capture the scintillation light generated during these events. This scintillation light might not directly reach the light sensors, but interact with the detector's internal surfaces where it can be absorbed or reflected. Since efficient light detection is crucial for the experiment's sensitivity, determining the reflectivity of the internal surfaces is essential for the high-precision light signal simulations required in this large-scale experiment.

The goal of this project is to determine the reflectivity of material samples from DUNE. Since LAr scintillation light has a wavelength of 128 nm, which falls within the vacuum ultraviolet (VUV) range, conducting light measurements requires a vacuum environment. The measurements are performed with the Vacuum Ultraviolet Light Characterization at Nikhef (VULCAN) setup, which is designed for light measurements in the VUV range. The first phase of the project consists out of commissioning the VULCAN setup and designing a system to read out the light signal. The second phase consists out of calibrating a reflection standard for VUV wavelengths to use as a reference for reflectivity measurements, and the actual reflectivity measurements on the samples. The reflectivity was assessed at wavelengths of 122 nm, 128 nm, 138 nm, and 175 nm.

Acknowledgements

I would like to express my gratitude to dr. Tina Pollmann for giving me the opportunity undertake my Master's project within the Dark Matter group. I'm grateful for her trust in me, especially given my background in energy and sustainability physics. While this is a field I believe is very important, this project allowed me to further explore my always existing interest in fundamental physics. I feel very thankful to have had such a valuable learning experience under her guidance.

I would like to thank Marjolein and Vikas for their continuous availability and their willingness to answer all my questions and guide me through the process. Marjolein's knowledge about VULCAN and Vikas' support with my coding were invaluable, and I could not have completed this project without their help.

I would also like to thank professor Paul de Jong for taking his valuable time to attend my presentation and examine my thesis, and Julio Acosta for his patience and pleasant collaboration.

Finally, I would like to thank the entire Dark Matter group for creating such a positive environment. Their support and interest in my project helped eased any insecurities and made me feel very welcome.

Contents

1

Introduction

In the Standard Model of elementary particles, neutrinos are regarded as some of the most interesting and mysterious particles. Neutrinos are fermions with no electric charge and an extremely small mass that interact solely through the weak nuclear force. They are one of the most abundant particles in the universe, far more abundant than the electrons and protons that form the atoms around us (1). Despite their vast presence in our universe, their existence was only hypothesized in the 1930s (2). Because they are so weakly interacting, it is incredibly difficult to detect them. This makes it challenging to study their behavior. A better understanding of the neutrino particle could possibly unlock answers to some of the biggest questions in particle physics and give more insight into the mysteries of the universe.

One of the major initiatives to detect and study neutrinos is the Deep Underground Neutrino Experiment (DUNE). DUNE is an international collaboration that is currently focused on constructing a neutrino detector at the Sanford Underground Research Facility (SURF) in Lead, South Dakota. This detector is located underground to shield it from cosmic background radiation that could interfere with the measurements. It is being built in the line of an intense neutrino beam generated by a particle accelerator at the Fermilab in Batavia, Illinois, situated approximately 1300 km away (3).

The DUNE detector will use a very large time-projection chamber (TPC) filled with liquid argon. When neutrino particles weakly interact with argon atoms, it often results in the creation of charged particles. These charged particles travel through the liquid argon in the TPC, resulting in ionization of argon atoms. Detection of the ions indicates a neutrino event. The charged particles can also provide the energy to excite argon atoms. As the excited electrons fall back to their ground state, they emit light. This light is called scintillation light. Liquid argon scintillation light has a wavelength centered around 128 nm

(4). This light travels through the liquid argon and will eventually be captured by DUNE's photodetectors. Capturing this scintillation light is crucial for detecting and analyzing neutrino interactions within the detector. By analyzing the signal from the photodetectors, it is possible to reconstruct the properties of the neutrino and the interaction that caused it.

The efficiency of light detection in the DUNE detector is a very important factor in its performance. The scintillation light that travels through the detector may not directly reach the photodetectors. It can interact with the detector's other internal surfaces where it can be absorbed, transmitted or reflected. Highly reflective surfaces increase the likelihood of scintillation light eventually reaching the photodetectors. The reflectivity of the materials used for DUNE's internal surfaces directly affects the amount of light that will be captured by the photodetectors, and therefore the overall sensitivity of the detector. Understanding the internal material properties is crucial as it enables more accurate simulations and calibration of the detector's response to argon scintillation light.

This project addresses this challenge by utilizing the Vacuum Ultraviolet Light Characterization at Nikhef (VULCAN) experimental setup. VULCAN is designed to study the optical properties of material samples used in scintillation based detectors. It is able to measure the reflectivity of materials at vacuum ultraviolet (VUV) wavelengths, which is essential since the scintillation light of argon is within the VUV range. This is achieved by conducting the reflectivity measurements in a vacuum chamber to avoid VUV light absorption by air. The primary goal of this project is to complete the commissioning of the experimental setup and to measure the reflectivity of material samples from DUNE's internal surfaces. This makes it possible to have a comprehensive understanding of their reflective properties under the specific conditions of the DUNE experiment.

2

Background

2.1 The Neutrino

2.1.1 The Standard Model

The Standard Model of elementary particles is a framework that describes three of the four known fundamental forces; electromagnetism, weak force and strong force, and it classifies all known elementary particles. One class of elementary particles in the Standard Model are the neutrinos. This model has been constructed over several decades with the Higgs boson, predicted in the 1960's and finally discovered in 2012, as its latest addition (5)(6)(7). The Standard Model has been successful in experimental predictions and explained several physical phenomena. However the model is not complete. It does not include gravitation, the fourth fundamental force, and it does not explain certain observed phenomena such as dark matter.

2.1.2 The History of the Neutrino

The neutrino was first proposed by Wolfgang Pauli in 1930. He argued that there needed to be a neutral particle to uphold the laws of energy conservation, momentum conservation and spin conservation during β-decay reactions. β-decay is a radioactive decay reaction where an atomic nucleus emits a β-particle, which can be either a high-energy electron or a positron. At that time Pauli only knew β-decay as a reaction where unstable nuclei emit electrons. To satisfy the laws of conservation, another neutral particle had to be emitted. He initially called this particle a neutron (8). It was not until two years later that James Chadwick discovered another more massive neutral particle that we now know as the neutron (1). Since there now were two particles with the same name, Enrico Fermi renamed Pauli's particle the "neutrino". In 1934 he also introduced his theory of β-decay that unified the existence of Pauli's neutrino, Chadwicks neutron, and Dirac's positron (9). There are two types of β-decay reactions: β^+ decay and β^- decay. In β^+ decay a proton transmutes into a neutron, a positron and an neutrino ν, in this case an electron neutrino ν_e.

$$p^+ \rightarrow n^0 + e^+ + \nu_e \tag{2.1}$$

In β^- decay a neutron transmutes into a proton, an electron and an electron antineutrino $\bar{\nu}_e$

$$n^0 \rightarrow p^+ + e^- + \bar{\nu}_e \tag{2.2}$$

Despite advancements in physics, this theory remains relevant today. It provides the basis for understanding neutrino interactions, which continues to be used in current neutrino research.

2.1.3 Properties and Interactions

Neutrinos are neutral leptons with a very small mass that is six orders of magnitude smaller than the mass of an electron (10). Leptons are fermions, elementary particles with half integer spin that follow Fermi-Dirac statistics, that do not undergo strong interactions. Other examples of leptons are muon particles, tau particles and electrons. Since neutrinos are neutral they also don't undergo electromagnetic interaction. They exclusively interact through the weak nuclear force and gravity, with gravitational interactions occurring very rarely due to their very small masses. Because they rarely undergo interactions, they can pass through matter largely unimpeded.

Neutrinos exist in three different flavors: the electron neutrinos, muon neutrinos and tau neutrinos. They are named after the three charged leptons. Each neutrino also has an antiparticle called an antineutrino. These also exist in the three different lepton flavors. Neutrinos can oscillate between these flavors. An electron neutrino that is created in a β-decay reaction can behave as a muon or tau neutrino when it is detected later on. This phenomenon of neutrino oscillation indicates that neutrinos are not massless. Although we do not yet know the mass of a neutrino, we know that there are three discrete mass eigenstates in which neutrinos can exist. These mass eigenstates do not align with the flavor eigenstates. When a neutrino is produced in a flavor eigenstate, it is in a superposition of the three possible mass states. It exists in all three mass states with a specific probability. When the neutrino travels, the mass states interfere with each other which causes the neutrino to oscillate. This mechanism makes it possible for the neutrino to change from one flavor to another (11).

Understanding the behavior and the properties of neutrinos, including neutrino oscillations and neutrino masses, is essential for a better understanding of the fundamental nature of particle physics. It is observed that neutrinos and antineutrinos show different oscillation behaviors. This difference could provide valuable insights into the matter-antimatter asymmetry, also known as the CP violation (11). Additionally, neutrino research can help with solving other mysteries like the formation of the universe and the existence of dark matter.

2.1.4 Neutrino Sources

Neutrinos and antineutrinos originate from a variety of processes. These processes can be natural and artificial, occurring on Earth and in cosmic events. Examples of neutrinos from natural sources include geoneutrinos, produced by the decay of radioactive elements in the Earth such as uranium-238; atmospheric neutrinos, generated when cosmic rays interact with atoms in the atmosphere; and solar neutrinos produced through nuclear fusion in the Sun. Another natural neutrino source is supernova events. Around 99% of the binding energy of the collapsing core of a star is released as neutrinos. These neutrinos can escape the core faster than photons which allow them to serve as early indicators of a supernova event (12).

Examples of artificial neutrino and antineutrino sources are nuclear reactors and nuclear weapons, where they are generated during the beta decay of fusion and fission products. Particle accelerators create neutrinos during the decay of secondary particles that are generated by accelerating particles to high energies and colliding them with a target. Artificial neutrino sources allow us to generate and study neutrinos under controlled conditions.

2.2 Neutrino Detection

2.2.1 Time Projection Chamber

An effective method for detecting weakly interactive particles is to use a time projection chamber (TPC). A TPC is a particle detector filled with a medium subjected to a uniform electric field that can capture and analyze charged particles. When a charged particle enters the TPC, it ionizes the atoms of the medium and creates electron-ion pairs. Under the influence of the electric field, the ionized molecules and the electrons travel through the TPC in opposite directions. This process is illustrated in Figure 2.1. The electrons drift toward anode wire planes, each at different potentials and arranged in different orientation patterns as shown in Figure 2.2. The electrons pass through the planes and are collected in the outermost plane with the highest potential. This configuration makes it possible to capture the electron signals from different perspectives and reconstruct the electron path in the two dimensions perpendicular to the drift direction (3).

By also measuring the time it takes for the electrons to reach the anode it is possible to determine the distance the electrons have traveled. This is achieved by capturing scintillation light emitted following a particle event. This approach allows for the reconstruction of the particle event in three dimensions. More information about this scintillation-based method will be discussed in Section 2.3.

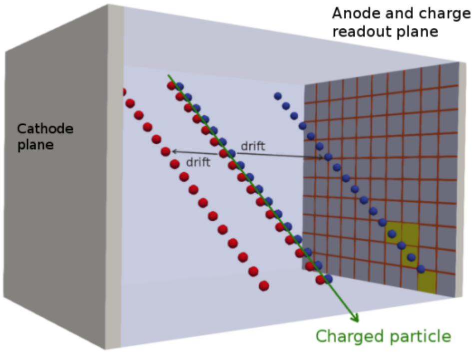

Figure 2.1: This figure illustrates the fundamental operation of a TPC. When a charged particle enters the TPC, it ionizes the atoms of the detection medium, creating electron-ion pairs. Under the influence of an electric field, the electrons and ionized molecules move in opposite directions to the cathode and anode planes. (13)

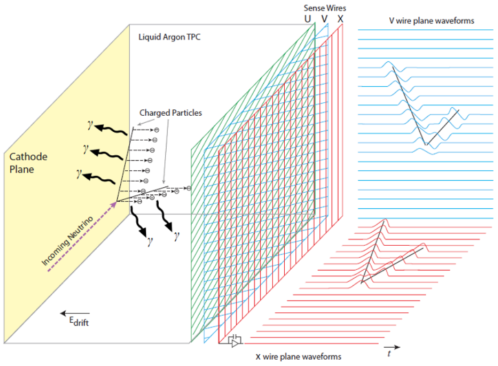

Figure 2.2: The configuration of anode wire planes in a TPC. This arrangement allows for electron capture from multiple angles and the reconstruction of the electron path. (14)

2.2.2 LAr as Detection Medium

Section 2.2.1 discussed the workings of TPCs and their application in detecting charged particles using a specific medium. This chapter will focus on a specific type of TPC, the liquid argon time projection chamber (LArTPC), that is particularly effective for neutrino detection. LArTPCs provide excellent spatial and energy resolution, allowing us to reconstruct the interactions of neutrinos in three dimensions with high accuracy. Argon is a noble gas that is abundant in earth's atmosphere. It is gaseous at room temperature and has a boiling point of 87.3 K. When neutrinos enter the liquid argon (LAr) medium inside a LArTPC, they can collide with argon atoms. During these collisions, the neutrinos interact with the argon atom via the weak nuclear force, which can produce secondary particles. These interaction are of the form:

$$v_l + \mathrm{Ar} \rightarrow l + hadrons + X \tag{2.3}$$

Here, v_l is a neutrino with a specific leptonic flavor, Ar is the argon nucleus, l is a charged lepton, hadrons refer to all other outgoing particles such as neutrons, protons, and mesons, and X represents the remnant nucleus (15). An example of a possible neutrino-argon interaction reaction is shown in Figure 2.3. The secondary particles that are produced during these interactions can cause ionization as they travel through the LAr. They possess enough energy to knock the electrons out of the argon atoms, creating the ion-electron pairs needed for TPC detection.

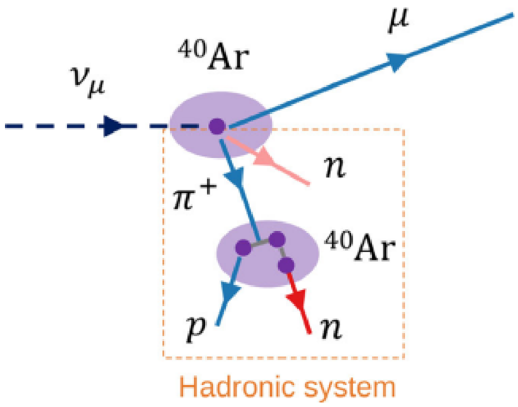

Figure 2.3: An example of a (muon) neutrino interaction within a LArTPC. This reaction results in the production of a muon and a hadronic system consisting out of hadrons and the remnant nucleus. (15)

One of the main advantages of LArTPCs is their capability to capture scintillation light. Secondary particles can excite the argon atoms. In this case, the electrons are not removed from the atom but excited to higher levels. When the excited electrons return to their ground state, they release their energy in the form of photons. This light, emitted by a material after absorbing energy from high–energy particles, is called scintillation light. For LAr the wavelength of scintillation light is centered around 128 nm, which is in the vacuum ultraviolet, or VUV range (4). The ability to measure both scintillation light and ionization signals allows for more precise energy resolution and better event reconstruction. Both mechanisms are illustrated in Figure 2.4. Besides the fact that LAr is a good scintillator, it also has a high light yield that is proportional to the energy of the incoming particles (16)(17). This relationship allows for accurate measurements of the particles energy.

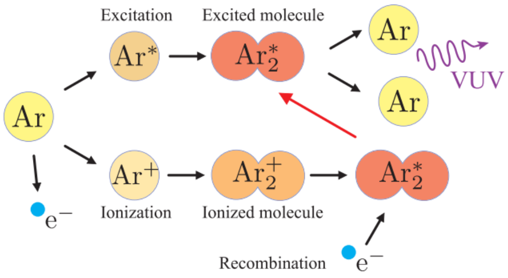

Figure 2.4: An overview of the ionization and scintillation processes in LAr. (4)

When a particle interacts with argon and causes scintillation or ionization, it is ideally the result of a neutrino interaction. LAr has low levels of radioactive isotopes. This minimizes background signals that could interfere with neutrino detection. As shown in Figure 2.5, the two unstable isotopes that are not negligible are ^{39}Ar and ^{42}Ar. These isotopes are produced by interactions with cosmic rays. To mitigate their presence, argon used for detection experiments is extracted from underground sources (18).

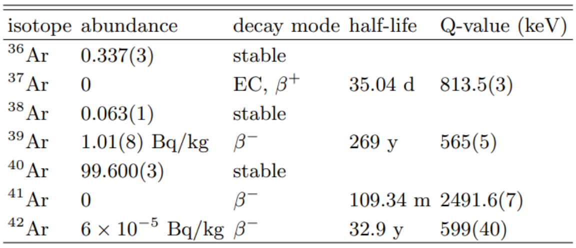

isotope	abundance	decay mode	half-life	Q-value (keV)
^{36}Ar	0.337(3)	stable		
^{37}Ar	0	EC, β^+	35.04 d	813.5(3)
^{38}Ar	0.063(1)	stable		
^{39}Ar	1.01(8) Bq/kg	β^-	269 y	565(5)
^{40}Ar	99.600(3)	stable		
^{41}Ar	0	β^-	109.34 m	2491.6(7)
^{42}Ar	6×10^{-5} Bq/kg	β^-	32.9 y	599(40)

Figure 2.5: Argon isotopes. (17)

Another key property that makes LAr suitable as a medium for neutrino detection is that it allows for pulse shape discrimination (PSD) between neutrino events and background noise. When a particle collides with the nucleus of an argon atom, it transfers energy and momentum to the atom causing excitation and ionization. It makes the atom move or "recoil". This effect is called nuclear recoil (NR). Similarly, when background events such a β-rays interact with the electrons in argon atoms, this can also cause ionization and scintillation, which is referred to as electron recoil (ER). Upon excitation, argon atoms can can form singlet $^1\Sigma_u^+$ and triplet $^3\Sigma_u^+$ excimer states. These states have a different decay time (17). The singlet excimer state has a decay time of about 6 ns. The triplet excimer state has a decay time between 1300 and 1600 ns, leading to a delayed scintillation signal (19). The ratio distribution of the singlet and triplet state excimers differs between NR and ER events. The scintillation signals from NR and ER therefore have distinct time profiles which allows for discrimination between neutrino event signal and background noise. By identifying and reducing background noise from radioactive decays, the overall accuracy of the neutrino detection can be significantly improved.

2.2.3 DUNE

One of the most ambitious large-scale projects in neutrino research is the Deep Underground Neutrino Experiment (DUNE). The DUNE collaboration is a global initiative with more than 1000 scientists and engineers from 31 countries. The experiment consists of massive LArTPCs containing a total of 40 kilotons of LAr (3). DUNE is a major step forward in neutrino research and particle physics as a whole.

DUNE is designed to study the properties and the behavior of neutrinos including their flavors, the mass eigenstates and the mechanisms behind neutrino oscillations. The neutrinos for the DUNE experiment will be produced at the Fermi National Accelerator Laboratory (Fermilab) in Batavia, Illinois. A proton accelerator generates neutrinos that will travel approximately 1300 kilometers underground in the direction of the LArTPCs at SURF. The Long-Baseline Neutrino Facility (LBNF) provides the infrastructure that supports the entire process of producing, transporting, and detecting neutrinos over this distance. Together with LBNF, DUNE will also work on creating the world's highest-intensity neutrino beam at Fermilab in order to improve the experiment (20). The DUNE detectors will consist of a near detector and a far detector, both shown in Figure 2.6. The near detector is positioned at 574 m from Fermilab (3). This detector will characterize the initial neutrino beam. The far detector at SURF will capture the neutrinos after they have propagated through the Earth. By comparing the neutrino beam compositions of the near and the far detector, it is possible to study the neutrino oscillations and the differences in the oscillation patterns of neutrinos and antineutrinos.

Another secondary goal of DUNE is to detect neutrinos emitted by supernovae. The LArTPCs are designed to capture the burst of neutrinos that would be emitted during a supernova explosion. This makes it possible to observe these events and learn more about the formation of neutron stars and black holes. Additionally, DUNE will search for proton decay. This phenomenon is predicted by several theories but never observed (21). The underground LArTPC shields the experiment from cosmic background noise, making it suitable for detecting rare events like proton decay.

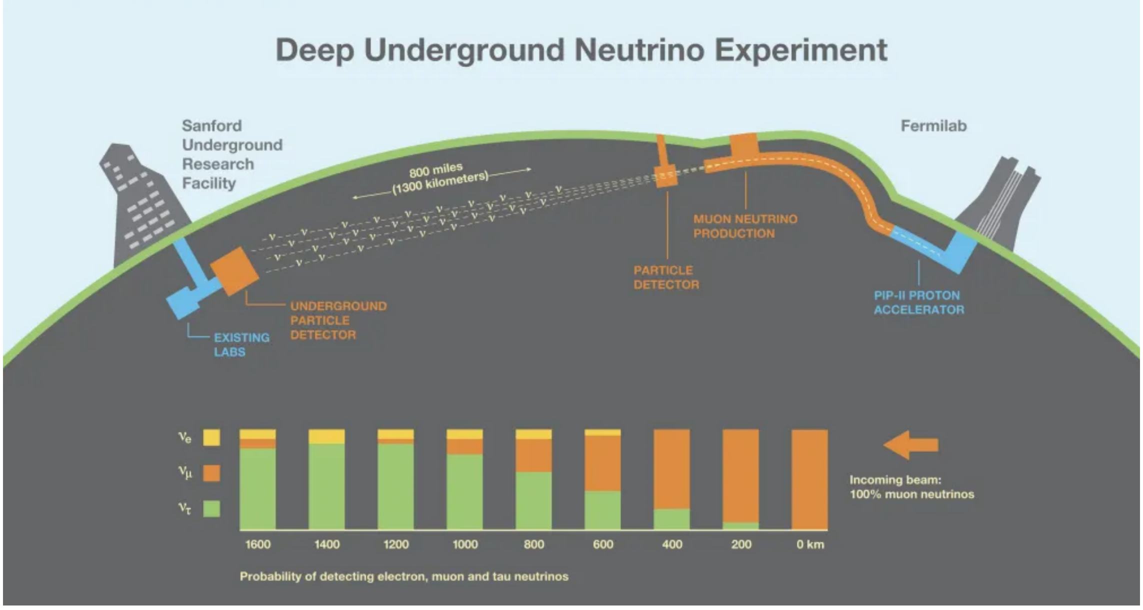

Figure 2.6: An illustration of DUNE. A muon neutrino beam created at Fermilab is detected by the near detector and travels through the Earth towards the far detector at SURF. By the time of arrival the neutrinos in the beam will be detected as mainly tau neutrinos. (22)

The first data collection with DUNE is scheduled to be in 2028. Before DUNE becomes fully operational, there are a number of prototype experiments being conducted at CERN. These experiments are called ProtoDUNE. They are designed to test the performance of DUNE technologies under the conditions similar to the expected conditions at DUNE. The insights obtained and challenges encountered during ProtoDUNE tests will help to improve the performance of DUNE at SURF. In April 2024, ProtoDUNE started filling the LArTPCs with liquid argon for a second run (23). Figure 2.7 shows photos from the inside of ProtoDUNE before and during this process.

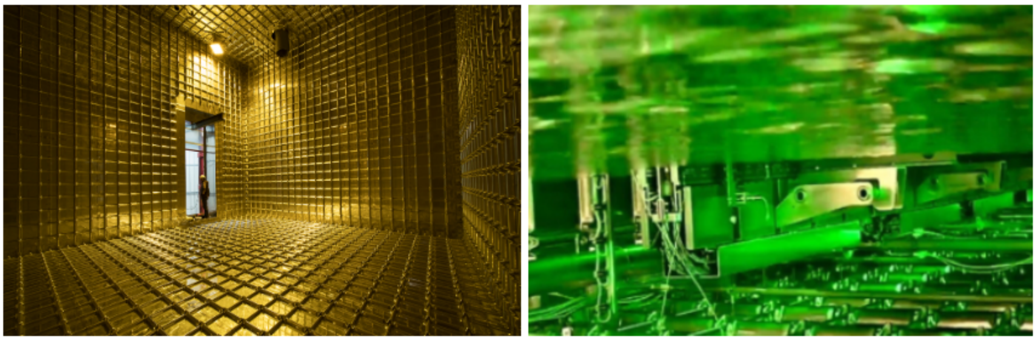

Figure 2.7: Photographs of ProtoDUNE at CERN. The left image shows the inside of an empty LArTPC. The right image shows a LArTPC in the process of being filled with liquid argon. (23)

2.3 Scintillation Light Detection in DUNE

2.3.1 Reflection, Absorption and Transmission

Efficient capture of LAr scintillation light inside the DUNE detector is essential for precise neutrino detection. To achieve this, the photons need to reach the photodetectors with minimal losses. When scintillation light travels through the LAr medium and interacts with materials inside the detector, it can be reflected, transmitted, and absorbed. Ideally, when the photons encounter DUNE's inner materials, they are reflected toward the photodetectors. The reflectance of light at the interface between these inner materials and the LAr can be calculated by the Fresnel equations:

$$R = \frac{R_\perp + R_\parallel}{2} \tag{2.4}$$

$$R_\perp = \left| \frac{n_1 \cos\theta_i - n_2 \cos\theta_t}{n_1 \cos\theta_i + n_2 \cos\theta_t} \right|^2 \tag{2.5}$$

$$R_\parallel = \left| \frac{n_2 \cos\theta_i - n_1 \cos\theta_t}{n_2 \cos\theta_i + n_1 \cos\theta_t} \right|^2 \tag{2.6}$$

Here, $R_\perp$ is the reflection coefficient for s-polarized light and $R_\parallel$ for p-polarized light, n_1 and n_2 are the refractive indices of the two media, θ_i is the angle of incidence, and θ_t is the angle of transmission. This angle can be calculated by Snell's law:

$$n_2 \cos\theta_i = n_1 \cos\theta_t. \tag{2.7}$$

The amount of scintillation light that is absorbed in the detector significantly impacts the amount of light that reaches the photodetectors. LAr is highly transparent to its scintillation light. The absorption in a medium can be calculated using the Beer-Lambert law:

$$A = \epsilon(\lambda)cx, \tag{2.8}$$

where A is the absorption, $\epsilon(\lambda)$ the molar absorption coefficient, c the molar concentration and x the distance the light travels in cm. From this law it is possible to derive the Beer-Lambert-Bouguer, or Attenuation law

$$I = I_0 e^{-\mu(\lambda)x}, \tag{2.9}$$

where I is the light intensity and $\mu(\lambda)$ is the light attenuation coefficient (24). This law gives the exponential decay of light intensity as it propagates through a material.

While low absorption and high reflectivity is generally desirable, for certain materials, minimizing reflectivity is crucial. This is the case for materials that should transmit the light, such as optical windows in front of photodetectors. Since

$$1 = \text{Reflectance} + \text{Transmittance} + \text{Absorption}, \tag{2.10}$$

the transmittance can be expressed in terms of the absorption coefficient and the reflectance:

$$T = e^{-\mu x} - R. \tag{2.11}$$

When considering reflection, there is a difference between specular and diffusive reflection. Specular reflection occurs when light reflects off a smooth surface, preserving the angle of incidence and resulting in a clear reflection, similar to a mirror. Diffusive reflection happens when light hits a rough surface, scattering in many directions. It can also happen when light passes into a translucent material that scatters the light before it exits. Understanding these types of reflection is important for optimizing the design of the detector components. Materials with high specular reflectivity can direct more light toward the photodetectors, while diffusive surfaces can help scatter light to enhance detection over a larger area.

2.3.2 Silicon Photon Multipliers

The scintillation light inside the DUNE detector is captured by silicon photon multipliers (SiPMs), advanced photon detectors known for their high sensitivity and performance in detecting low levels of light. SiPMs are composed of a 2D array of parallel connected microcells on a silicon substrate. Each microcell contains a single-photon avalanche diode (SPAD) and a quenching resistor (R_Q). Figure 2.8 shows how the microcells are connected on the silicon. Figure 2.9 shows a photograph of the SiPMs that are used in the VULCAN experiment.

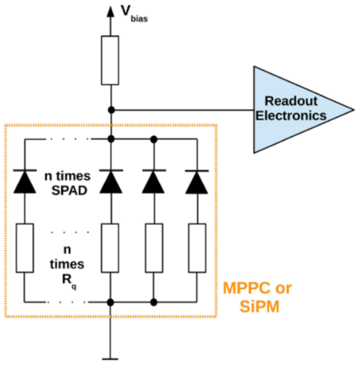

Figure 2.8: Simplified circuit diagram of a SiPM with parallel connected of microcells consisting out of a quenching resistor and a SPAD. (25)

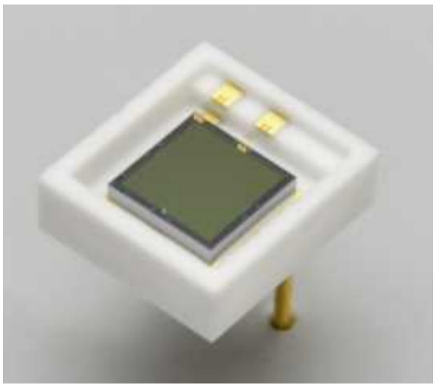

Figure 2.9: The Hamamatsu VUV-MPPC S13370-3050CN silicon photon multiplier that was used in the experimental setup for this project. (26)

The SPADs inside the SiPM act as silicon diodes. Silicon is a semiconducting material with four electrons in its valence band. These electrons form covalent bonds with neighbouring silicon atoms to create a lattice structure. Introducing atoms with five valence electrons in this lattice, causing a free excess electron, is called n-type doping. Introducing atoms with three valence electrons results in a "hole" in the lattice. This is called p-type doping. If both p-doped and n-doped silicon are put together their interface is called a p-n junction. This junction is a diode since current can only flow in one direction. The electrons in the n-doped silicon flow to the holes in the p-doped silicon, leaving a positive charge on the n-type side and a negative charge on the p-type side. This region of charge separation is called the depletion layer. The process is shown in Figure 2.10a.

When a forward voltage bias (V_{BIAS}) is applied, with a positive potential on the p-type side of the diode, the depletion layer narrows and current can flow. When a reverse V_{BIAS} is applied, the depletion layer widens and current cannot flow. These scenarios are illustrated in Figures 2.10b and c. If a reversed V_{BIAS} is applied and a photon is absorbed in the depletion layer, it knocks out electrons in the silicon creating electron hole pairs. This is called impact ionization. The reverse V_{BIAS} sets up an electric field that accelerates the holes to the p-type region and the electrons to the n-type region, resulting in a current flow.

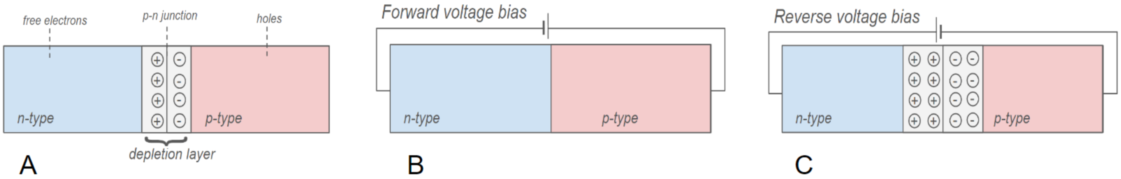

Figure 2.10: (a) Simplified illustrations of the mechanism inside a diode with p-doped and n-doped material. (b) When a forward voltage bias is applied the depletion layer closes and current can flow. (c) When a reverse voltage bias is applied, the depletion layer widens and current can no longer flow.

If the reverse V_{BIAS} is increased past the breakdown voltage (V_{BR}), the diode normally stops conducting. In a SiPM, the diode enters the Geiger mode (27). If a photon is absorbed by a SPAD operating in Geiger mode, the charge carriers are accelerated to such an extend that they generate secondary charge carriers through impact ionization. The electric field in this region is strong enough to accelerate these secondary charge carriers to generate even more charge carriers. This process is called the avalanche effect and it is illustrated in Figure 2.11. The ionization avalanche is spread throughout the silicon that is under the influence of the electric field and the silicon becomes conductive. It will continue to generate current until it is "quenched".

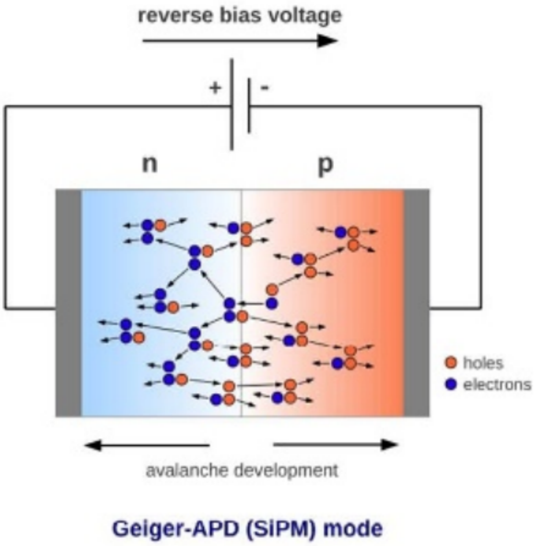

Figure 2.11: SPAD operating in Geiger mode. When a voltage bias above V_{BR} is applied, the strong electric field accelerates the charged particles, causing an avalanche effect. (25)

Each charge carrier that is generated by impact ionization can generate new charge carriers. This means that the avalanche effect can continue forever if it is not quenched. The quenching mechanism is designed to stop this effect by reducing the voltage to below V_{BR}. This effect is depicted in the typical SPAD signal waveform presented in Figure 2.12. Before the SPAD operating in Geiger mode absorbs a photon, the voltage is at the V_{BIAS} level and there is no current flowing. When a photon hits, the avalanche effect causes a current. This happens at the beginning of the waveform t_i. The highest point of the waveform i_{max} is the maximum current that the SPAD can generate. The current flows through the R_Q in the microcell which causes the voltage to drop. When it drops below the V_{BR}, the avalanche can no longer sustain itself and stops. The current decrease exponentially until there is no current flowing. The voltage returns to V_{BIAS} and the SPAD can detect another photon.

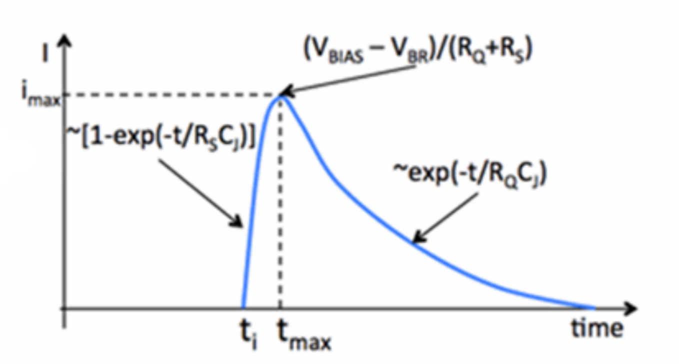

Figure 2.12: SPAD signal waveform representing a photon peak. When a photon is detected, the avalanche effect generates a current that reaches its maximum value at i_{max} before being quenched by the quenching resistor. The quenching causes the voltage to drop below the V_{BR} which causes the avalanche to stop and the current to exponentially drop.(28)

Each SPAD can detect the presence of photons but it cannot quantify the amount of photons that were absorbed. When a single microcell in the SiPM detects multiple photons simultaneously, the resulting waveform is indistinguishable from the waveform that occurs after a single photon event, known as a 1 PE (photoelectron) peak. By combining multiple microcells in an array, the SiPMs can detect multiple single photons at the same time. If two photons are detected by two different SPADs, their waveforms combine and create a 2 PE peak. This 2 PE peak has the same shape but a higher amplitude. The same thing happens when more than two photons are detected, resulting in 3 PE peaks and so on.

2.3.2.1 Dark Counts

Besides photon signals, SiPMs can also produce dark count signals. Dark count signals are noise signals that reduce the sensitivity of the detector. Therefore, it is important to minimize the dark count rate (DCR), especially when detecting low levels of light. Dark counts are mainly caused by thermal excitations. Thermal energy can make the valence electrons in the silicon lattice excite and create electron-hole pairs. These charge carriers can also generate an avalanche effect, resulting in a current flow that is indistinguishable from a photon-induced current flow. Higher temperatures increase the amount thermal excitations. To calculate the relation between the temperature and the DCR we use the equation

$$k = Ae^{-\frac{E_a}{RT}}, \tag{2.12}$$

where k is the DCR constant, A is a pre-exponential factor called the Arhennius factor, E_a is the activation energy that is related to the energy gap between the valence band and the conduction, R is the gas constant, and T is the temperature (29). The DUNE detector SiPMs operate at low temperatures to minimize the effect of thermal dark counts.

Another cause of uncorrelated noise is quantum tunneling (30). Electrons pass through the potential barrier at the p-n junction in the SPAD, creating electron-hole pairs that can initiate the avalanche effect. Thermionic dark count noise and quantum tunneling both contribute to the DCR. A third source of noise is after-pulsing (31). After pulsing happens when charge carriers become trapped in impurities in the silicon lattice. When they are released, they can generate a new avalanche effect. Since this noise is correlated with photon detection it is not classified as dark counts, but it still contributes to the noise level. By using high-purity silicon to reduce the number of impurities and optimizing the electrical field to prevent quantum tunneling, the background noise can be further minimized, increasing the sensitivity of the DUNE detector

3

VULCAN Setup

3.1 VULCAN Project

As described in Section 2.3.2., the scintillation light that is produced after a neutrino event can be detected by the SiPMs in the LArTPC. This scintillation light scatters in all directions. Some photons might not fall onto a SiPM but on another part of the detector's interior. Depending on the material properties these photons can be absorbed, transmitted, or reflected. Ideally these photons will be reflected so they can still be captured by a SiPM. The VULCAN project, short for Vacuum Ultraviolet Light Characterisation At Nikhef, was created to measure how materials from particle detectors will behave. With the VULCAN experimental setup we aim to learn more about the optical properties of materials used in scintillation based TPCs. The setup is able to simulate light with a specific wavelength and analyze how material samples behave when they are exposed to this light. The project started in 2021 with the design of the setup. Calibration measurements have been conducted in the following years, but no successful reflection measurement has been conducted yet. The goal of this project is to measure the reflectivity of materials that are used in DUNE's interior when exposed to liquid argon scintillation light.

3.2 Experimental Setup

The main components of the VULCAN experimental setup, also referred to as the Vacuum Ultraviolet setup or VUV setup, are the deuterium lamp, the monochromator, the vacuum sample chamber and the vacuum pump. The deuterium lamp is the light source that creates a light beam. The monochromator disperses this light beam and isolates light of a specific wavelength. This makes it possible to reproduce the LAr scintillation light of

128 nm wavelength. The vacuum pump creates a necessary vacuum in the vacuum sample chamber. Figure 3.1 shows how these components are assembled on a table. The inside of vacuum chamber setup is designed so that both the reflection and transmission of samples can be measured. This is done by placing the sample in a sample holder that can rotate around its own axis, and the light sensors on an arm that rotates around the sample holder. These designs are developed and constructed by Jeroen van den Borgh and Casimir Post (32).

To read out the SiPM signal, a data acquisition (DAQ) system is designed. The SiPMs are powered by a bias voltage through a readout box located outside the vacuum chamber. This box is used to amplify and convert the SiPM signal before it is send to the digitizer and finally the lab computer. An external trigger is applied to the digitizer. Additionally, the temperature and pressure data from inside the vacuum chamber are collected and sent to the lab computer. A digital drawing of the main components of the VUV setup is shown in Figure 3.1. More detailed descriptions of these components will be given in the following sub-sections.

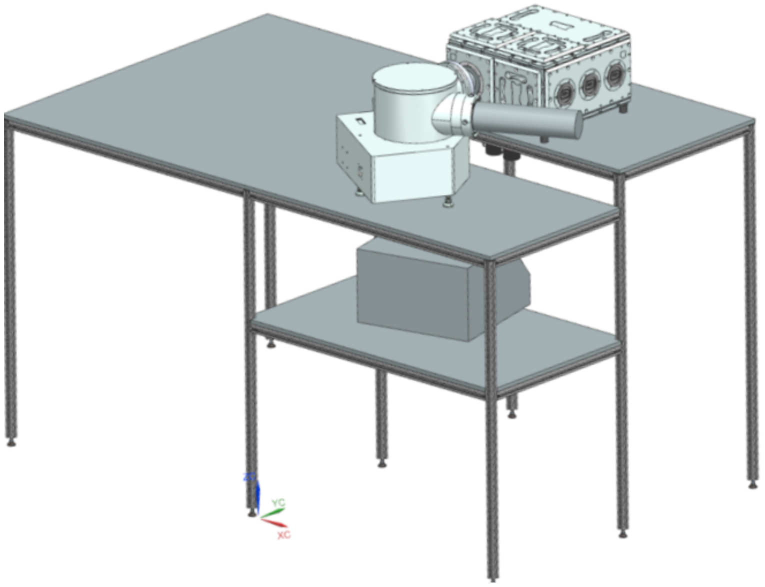

Figure 3.1: CAD drawing of the VUV setup design. This drawing shows the specially designed setup table with the vacuum chamber, the monochromator, the deuterium lamp and the vacuum pump. (32)

3.2.1 Vacuum Sample Chamber

In order to achieve the vacuum that is required for this experiment, the Ideal Vacuum $6 \times 12 \times 12$ "Short Cube" Modular Vacuum Chamber shown in Figure 3.2 is used. This modular system consists of a frame with different sized plates that can be replaced by customized plates with specific modifications. This is very convenient for this experiment because it allows for easy adjustments to meet setup requirements.

As shown in Figure 3.2 there are several customized plates installed on the vacuum chamber. One of the side plates has an opening that is connected to the monochromator, deuterium lamp and the vacuum pump stage. The side plate to the left contains two D-sub feedthroughs. One of these feedthroughs connects the SiPMs inside the chamber to the DAQ system while the other connects a PT100 temperature sensor (Heraeus 1PT100 KN1510 probe sensor) to a temperature readout box. The plates on top of the chamber contain an opening that is connected to the Pfeiffer MPT 200 AR full range pressure sensor, an Ideal Vacuum vent valve, and an Ideal Vacuum liquid nitrogen trap. The latter will be used in future experiments that require cooling. At the bottom of the chamber, two rotary feedthroughs are installed for the sample holder and the SiPM holder. The side plate on the right is equipped with fastening bolts with knobs. This is for convenient and quick assembly of the chamber to make changes in the setup and to swap the sample.

Figure 3.2: (a) Right-side view of the vacuum chamber with the monochromator being the light blue object attached to the chamber. (b) From left to right the pressure sensor, the liquid nitrogen trap and the vent valve. On the left side plate the two D-sub connectors are visible. (c) Cutout in the setup table below the vacuum chamber that creates space for the rotary feedthroughs that control the sample holder and SiPM holder.

All the plates on the vacuum cube are sealed with Viton O-rings. Even if the vacuum chamber is completely sealed from its surroundings, the quality of the vacuum can be affected by outgassing. Outgassing is the process where materials inside the vacuum environment release trapped gasses. To minimize this effect, the components that are used inside the vacuum chamber are selected and designed to have minimal gas trapping, to create a more stable vacuum environment inside the chamber.

3.2.2 Sample Holder and SiPM Holder

The sample holder is designed to place material samples inside the vacuum chamber. The holder, constructed from copper due to its superior thermal and vacuum properties, is capable of holding two samples simultaneously. It is designed by Jeroen van den Borgh and refined and developed by Casimir Post. The holder is 9.2 cm long, 4 cm high, 1.8 cm thick and it can hold samples of 3 × 3 cm. It is symmetrical so that rotating it by 180° lets the two samples alternate with the exact same orientation and distance from the light source. This is necessary because each sample measurement needs to be calibrated by a reflection standard. A technical drawing of the sample holder is shown in Figure 3.3.

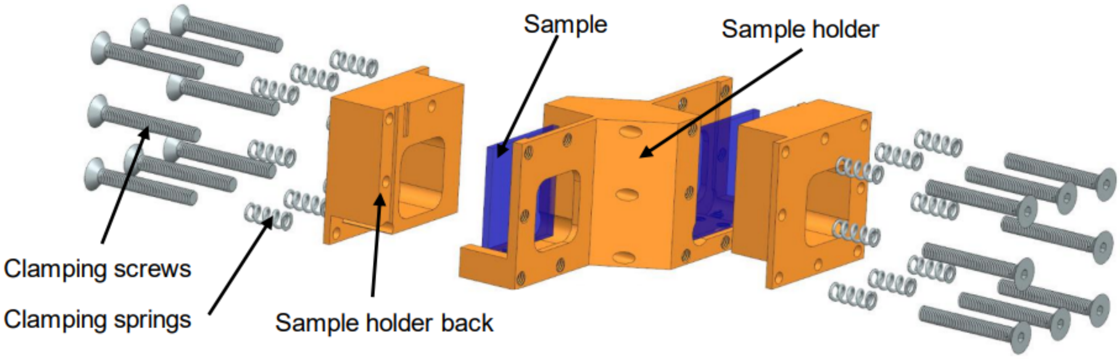

Figure 3.3: Drawing of the sample holder design with all parts, screws and springs. The samples are mounted from the back so the thickness of the sample does not affect the distance to the light source. (32)

The SiPM holder is placed at the end of a 13.5 cm rotatable arm that allows the light sensor to move over the sample holder without interference. It holds three Hamamatsu S13370-3050CN VUV-MPPC SiPMs, each with a photosensitive area of 3.0 × 3.0 mm. These SiPMs were selected for their sensitivity to VUV wavelengths, with a spectral response range spanning from 120 nm to 900 nm. By rotating the sample holder and the sensors and placing them in different orientations, it is possible to measure both reflection and transmission. For this project, only the the reflection configuration is used. In this setup the sample holder is placed at an angle of approximately 45 degrees relative to the light beam. A top view drawing for this setup is shown in Figure 3.4. Photographs of the inside of the vacuum chamber are shown in Figure 3.5.

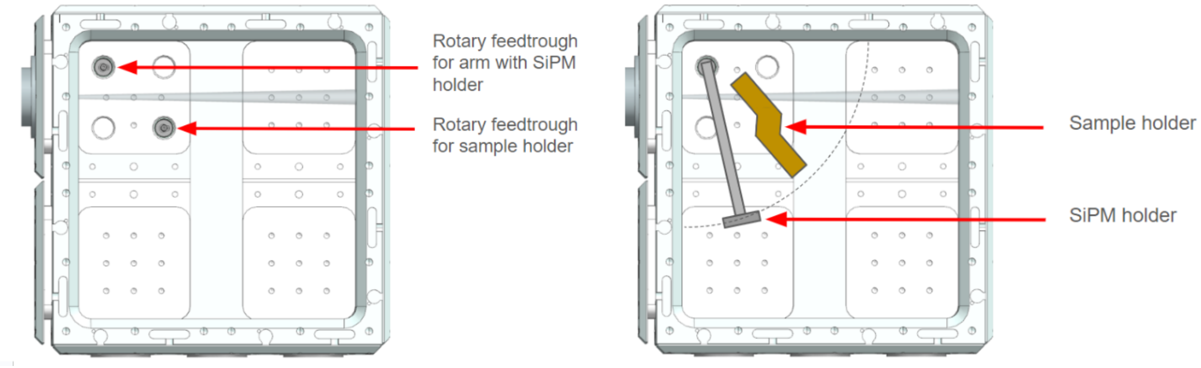

Figure 3.4: CAD drawing of the top view of the vacuum chamber. Adapted from (32)

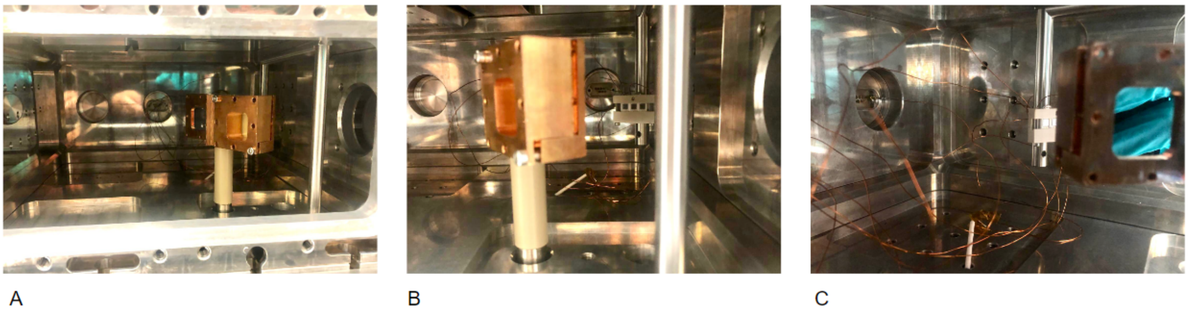

Figure 3.5: Photographs from inside the vacuum sample chamber where the sample holder and SiPM holder and the D-sub feedthroughs are visible. The white rod on the chamber floor in image (b) and (c) is the temperature sensor.

3.2.3 Light Source and Monochromator

The light source in the VULCAN setup is the Hamamatsu L15094 Deuterium lamp, shown in Figure 3.8. This lamp is specifically designed for experiments with VUV wavelengths. The main reason that this lamp is suitable for our experiment is because it has a window that is made out of magnesium fluoride (MgF_2). This material is highly transmitting for VUV wavelengths as opposed to glass or other window materials. The lamp operates by exciting molecular deuterium gas, which emits light as the atoms in the gas return back to their ground state. This emitted light covers a broad range of wavelengths from 115 nm to 400 nm (33). The intensity emission spectrum provided by Hamamatsu is shown in Figure 3.6. The 128 nm LAr scintillation light wavelength falls within this range, with a sufficient intensity output. Before this project the intensity spectrum was measured with the VULCAN setup by Jasmijn Stevens. The results given in Figure 3.7 show that this measurement matches the provided spectrum well. The discrepancy in the peak height around 160 nm is caused by SiPM saturation.

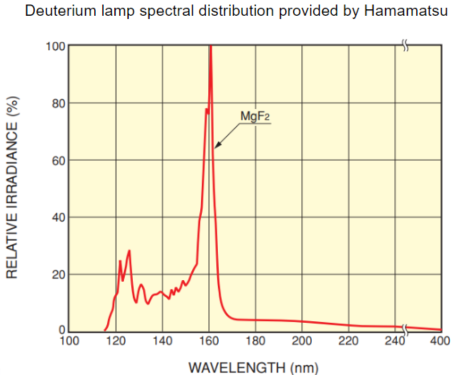

Figure 3.6: Deuterium lamp spectrum of model L15094 provided by Hamamatsu. (34)

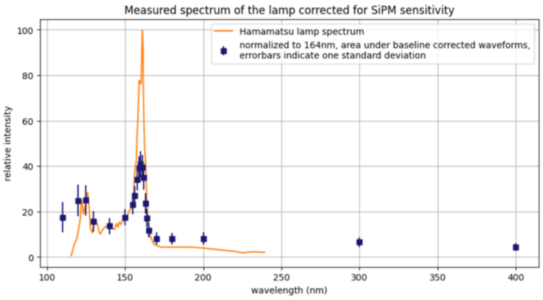

Figure 3.7: The measured deuterium lamp spectrum compared to the spectrum provided by Hamamatsu. Around the peak at 160 nm the SiPM saturation is visible. (35)

Because the lamp emits a broad range of wavelengths, a monochromator is used to isolate the wavelengths that are needed for the experiment. The McPherson 234/302 200mm focal length vacuum monochromator is used to narrow the deuterium lamp output to a specific wavelength. Figure 3.10 shows how the monochromator is attached to the lamp. The monochromator has a reflective grating of 1200 grooves per millimeter. It can achieve wavelength selection accuracy of 0.1 nm in the range of 30 nm to 550 nm. The grating is coated with aluminum and magnesium fluoride ($Al+MgF_2$) to enhance the reflection of VUV wavelengths with minimal loss (36).

The incoming light from the deuterium lamp falls on the grating and is diffracted into different wavelengths. These wavelengths are spread out spatially. That means that different wavelengths of light exit the grating at different angles. By rotating the grating, the monochromator aligns the selected wavelength with the exit slit. A higher groove density disperses the light more finely. This increases the spectral resolution, but reduces the spectral range that can be covered. Adjustments to the entrance and exit slit openings allow for fine-tuning of the beam size and intensity. The entrance slit mainly controls the light intensity, while the exit slit controls the accuracy of the selected wavelength by isolating a more precise segment of the spectrum. However, narrowing the exit slit also decreases the light intensity. Figure 3.9 shows a top view of the light path inside the monochromatic and Figure 3.10 shows an example of an experimental setup. This monochromator also features an aberration-corrected Seya-Namioka design to account for optical aberrations that cause the light rays to deviate from their path. This design ensures that the selected wavelength light is focused at the exit slit.

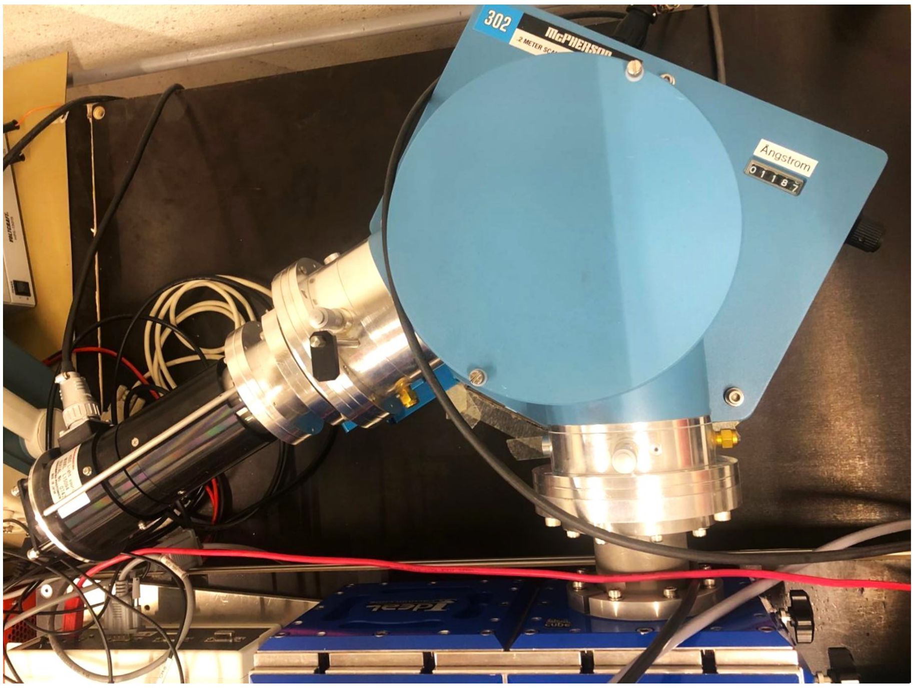

Figure 3.8: Photograph of the McPherson monochromator with the Hamamatsu deuterium lamp attached on the left. The window on the top right corner shows the selected wavelength in Angstrom.

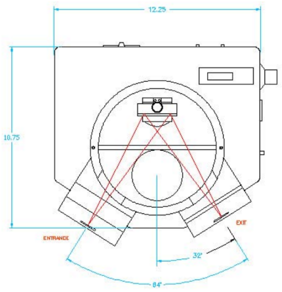

Figure 3.9: Top view drawing of the McPherson 234/302 monochromator. (36)

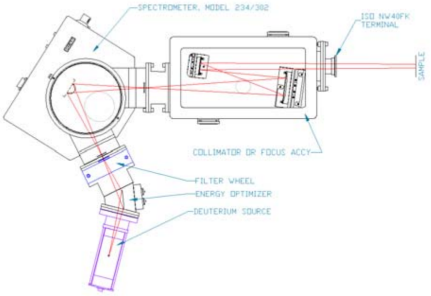

Figure 3.10: Example configuration for monochromator experimental setup. (36)

3.2.4 Vacuum Pump System

To achieve the vacuum level that is needed for this experiment, a vacuum pump is connected to the VUV setup. The pump that is used is the Pfeiffer Vacuum HiCube 80 Eco DN63. Under perfect conditions, this pump is capable of creating a pressure of 1×10^{-7} mbar in 557 seconds in a 10 L volume (37).

The vacuum pump system operates by using a combination of the MVP 015-2 diaphragm backing pump and the HiPace 80 turbomolecular pump. In the diaphragm pump a diaphragm oscillates to create alternating low and high-pressure zones in the pump chamber. This draws in air from the connected vacuum chamber through an inlet valve, and expels it through an outlet valve. When the pressure is reduced to around 5 mbar, the turbopump takes over. The turbopump has rotating blades that hit incoming gas molecules. This transfers momentum and creates a flow of gas directed out of the vacuum chamber.

Figure 3.11: Photograph of the Pfeiffer vacuum HiCube 80 Eco DN63 pumping station in the VULCAN setup

3.2.5 DAQ System

The data acquisition (DAQ) system is designed to accurately capture and process the signals generated by the SiPMs. This system includes a SiPM power supply, an amplification power supply, a readout system, a digitizer and an external trigger. A schematic drawing of the DAQ system is provided in Figure 3.12.

The Hamamatsu S13370-3050CN SiPMs are powered by a reverse V_{BIAS} through the readout system with the operating voltage (V_{OP}) set to 4 V above their breakdown voltage (V_{BR}), which will be determined in Section 5.2. When a SiPM detects a photon it generates a current signal. The readout system converts this current to a voltage signal suitable for processing by the digitizer. An amplifier operating at 7 V is used to enhance the signal strength since the initial SiPM signal is too weak for data analysis. The readout system is designed and developed by Julio Acosta over the span of several months. This process involved a lot of testing of different configurations to achieve the optimal performance for the VUV setup. Chapter 4 provides extensive details on this process.

The amplified and converted SiPM signal is digitized by the CAEN V1730 14 bit digitizer. This makes the signal readable by the computer for further analysis. When the system performs continuous data acquisition, the amount of data becomes too much for the digitizer to process, leading to system overload and shutdown. Therefore, an external trigger, set to 500 MHz, is applied to the digitizer. The digitizer is programmed to collect data in 30.14 microsecond intervals after every trigger to ensure that the system does not become overloaded.

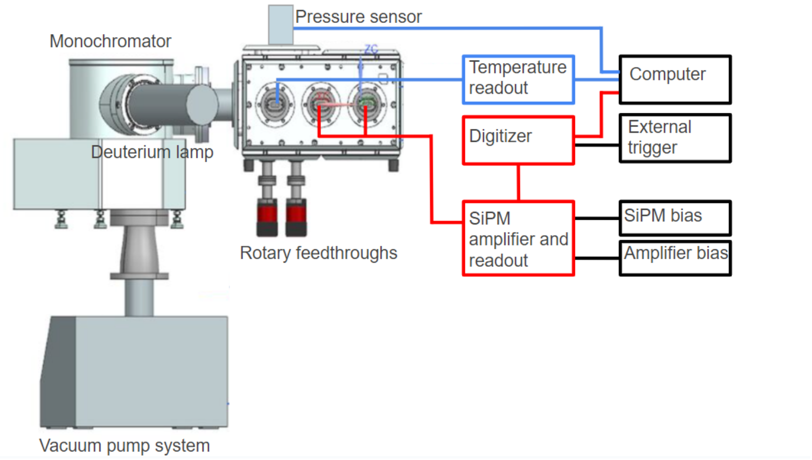

Figure 3.12: A schematic drawing of the complete VULCAN DAQ system including the temperature and pressure sensors. Adapted from (32)

4

SiPM Readout Electronics

Typically, SiPMs are directly mounted on a readout board. Because the electronics that are used in the readout system are not suitable for vacuum environments, it is not possible to place the readout board or even the amplification stage inside the vacuum chamber. Placing the readout system outside the vacuum chamber and connecting the SiPMs through a vacuum feedthrough via long wires was strongly discouraged, as it would be impractical and most likely infeasible to capture a clear signal. This unique challenge required the development of a custom readout system rather than purchasing a standard system, which significantly complicated the project.

A substantial portion of this project was dedicated to designing and testing different readout system prototypes. This was done in collaboration with Julio Acosta from the Nikhef electronics department. To conduct the reflectivity measurements, three SiPMs were integrated into the experimental setup, requiring three SiPM readout channels in the final readout system. Over several months, four different prototypes were tested to address the variations in conversion and amplification electronics, before determining the optimal configuration. This configuration was then replicated and installed in the readout box that was used for the measurements. A detailed explanation of the four prototypes is given in Section 4.2.

4.1 General Requirements and Considerations

SiPMs generate weak electrical signals, around 10 µA (38). These signals are often too small to be directly processed. A SiPM readout system is implemented to convert and amplify the SiPM signal so that in can be digitized and analyzed by the VULCAN DAQ system. Designing the readout system requires electronics with high bandwidth and low noise. The bandwidth refers to the ability of an electronic system to process signals in a given amount of time. A high bandwidth is necessary for the electronics to handle the rapid light signal pulses from the SiPMS, which typically fall within the range of 100 to 300 ns. The low noise is essential to not compromise the Signal-to-Noise Ratio (SNR).

The initial SiPM signal is an electrical current. In order to be processed by the DAQ system this needs to be converted to a voltage signal. This can be done by a shunt resistor that is followed by an amplification stage. The resistance needs to be carefully chosen. Increasing the resistance reduces the bandwidth resulting in a slower signal response. Lowering the resistance limits the ability to amplify the signal. An alternative option is a transimpedance amplifier. This type of amplifier directly converts current to voltage. It generally offers a higher SNR but it is more sensitive to instabilities and oscillations caused by parasitic effects. To minimize these issues, the amplifier should be placed as close as possible to the SiPM. Because the electronics are not suitable for vacuum environments, it is not possible to place them inside the vacuum chamber. Therefore, the readout system is placed outside the chamber and connected to the SiPM wires via a D-sub feedthrough. This also causes the system to be more vulnerable to instabilities and high frequency noise.

4.2 Prototype Design and Performance

4.2.1 Prototype 1

The first prototype readout system consisted of a readout box with eight identical configurations. A photograph of the inside of this box is shown in Figure 4.1. The circuit diagram of this configuration is shown in Figure 4.2. It makes use of a BUF602 buffer and two non-inverting OPA847 voltage amplifiers with an amplification gain of approximately 18. This configuration offered high bandwidth capabilities and relatively low noise levels. It was able to scale up 5 PE peaks to 2 volts which is the maximum input voltage of the CAEN V1730 digitizer. It was initially designed without the buffer but it was added due to occurring parasitic effects that could be attributed to the long wire to the SiPM and the cabling inside the box.

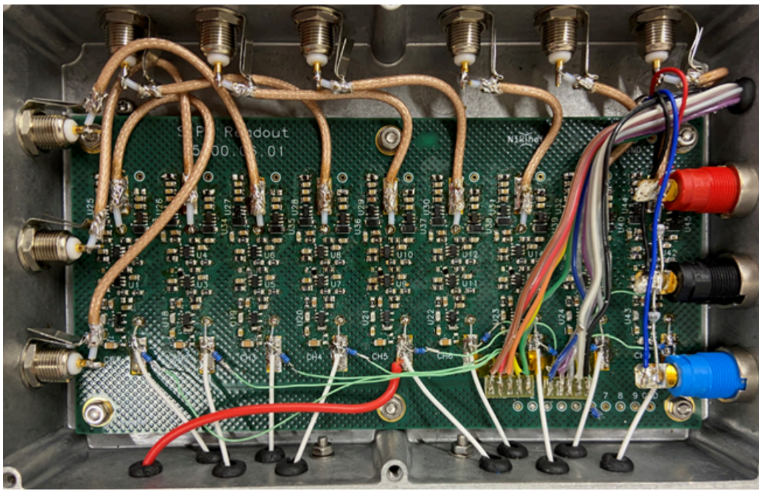

Figure 4.1: Top view photograph of the opened readout box with eight identical channels with the Prototype 1 configuration.

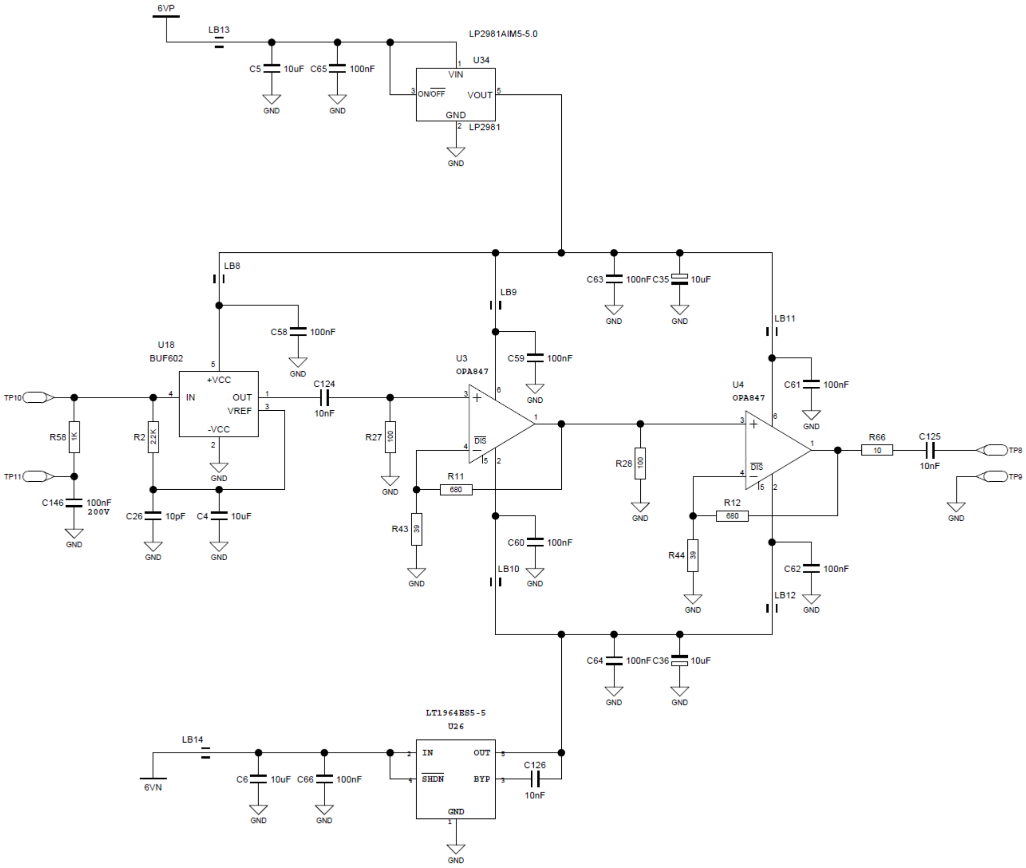

Figure 4.2: Circuit diagram of the Prototype 1 readout system configuration with BUF602 buffer and two non-inverting OPA847 amplifiers.

Signal traces that were taken with this configuration are shown in Figure 4.3. The prototype unfortunately did not meet necessary requirements but it did highlight the areas that needed improvement. The SNR of this prototype was low which made it difficult to extract and analyse the SiPM signal. Another issue that needed to be addressed for data analysis was the baseline shifting. This was caused by negative undershoot after signal peaks, and a slow readout tail that led to signal overlap. On top of that, the output signal saturated at random times and oscillated between the voltage limits damaging sensitive electrical components. This resulted in six of the initial eight channels in the readout box dying. The design for the newer prototypes was modified to improve the SNR, avoid the undershoot, enhance fast signal extraction and minimize the slow recharge tail.

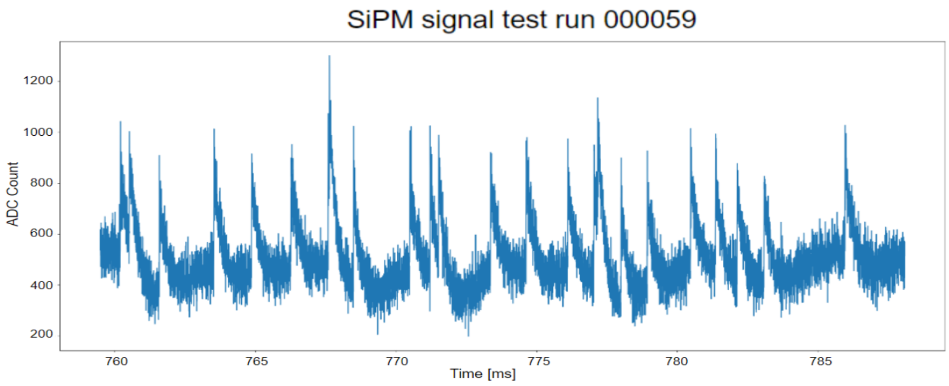

Figure 4.3: SiPM signal trace taken at VULCAN with the Prototype 1 readout system configuration showing low SNR and unstable baseline due to undershoot and slow recharge tails.

4.2.2 Prototype 2

In order to develop a better prototype, the influence of the buffer on the output signal was analyzed. This was done by using LTspice to simulate the behaviour of the SiPM circuit model (39). The simulations showed that the bandwidth of the initial prototype was limited due to the input resistance of the BUF602 buffer. This resistance combined with the SiPM's capacitance forms a low pass filter that acts as a barrier for the higher frequency components of the signal. A higher input resistance increases the current-to-voltage conversion, but also reduces the cut-off frequency of the filter. Simulations showed that beyond 50Ω the signal amplitude did not increase significantly but the bandwidth decreased. Therefore, the resistance was reduced from 2.2kΩ to 50Ω. This minimizes the recharge tail and fluctuations in the baseline.

The second main adjustment was the removal of one of the amplifiers. The OPA847 amplifier has a 200 MHz bandwidth which exceeds the signal bandwidth after the buffer stage. This excessive bandwidth caused unwanted high-frequency noise to be amplified by the two ($18x18$) amplifiers, causing the system to saturate. In order to avoid this, the second amplification stage was removed and the gain of the first amplifier was increased to 100. By increasing the gain, the range of frequencies the amplifier could handle was limited to about 40MHz. A passive second order low pass filter was added at the end of the circuit to reduce the noise even further.

Another measure to address the signal peak overlap and baseline shifting was the implementation of a high-pass filter to eliminate the slow signal components. This method introduced a large undershoot visible in Figure 4.4, that made data analysis more challenging. A technique called pole-zero cancellation was then implemented as an alternative. In this context poles are frequencies where the signal gets weaker, and zeros are frequencies where the signal gets stronger. By placing a zero at the same frequency as the pole created by the slow recharge tail, the impact of the pole gets cancelled out. This makes it possible to get rid of the slow signal components without causing undershoot.

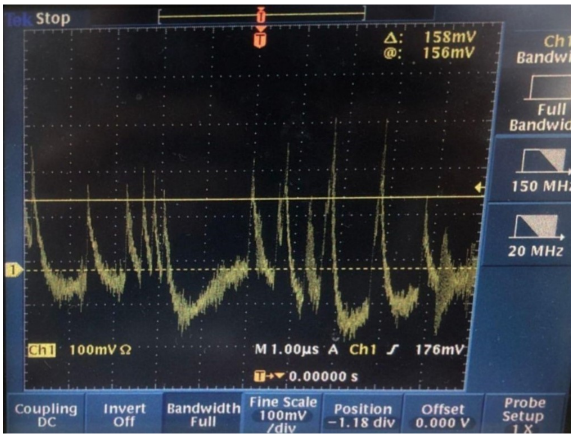

Coupling DC
Invert Off
Bandwidth Full
Fine Scale 100mV /div
Position −1.18 div
Offset 0.000 V
Probe Setup 1X

Figure 4.4: Oscilloscope screen showing SiPM signal with large undershoot due to the high-pass filter.

The final adjustment is in the buffer power supply. In the first prototype, the buffer was powered with a +5V single supply. It used the mid-point reference voltage for the AC input signal which split the +5V to create a ground reference. This setup allowed noise to enter the circuit through the mid-point reference. It was decided to remove this configuration and switch to a dual power supply that powers the buffer with positive and negative voltages.

The shortcomings of prototype 1 led to the improved design for the second prototype. Figure 4.5 shows the circuit diagram for the configuration of Prototype 2. The performance of this prototype is demonstrated by a dark count signal trace shown in Figure 4.6. Compared to Figure 4.3 we observe a significantly larger SNR and a more stable baseline.

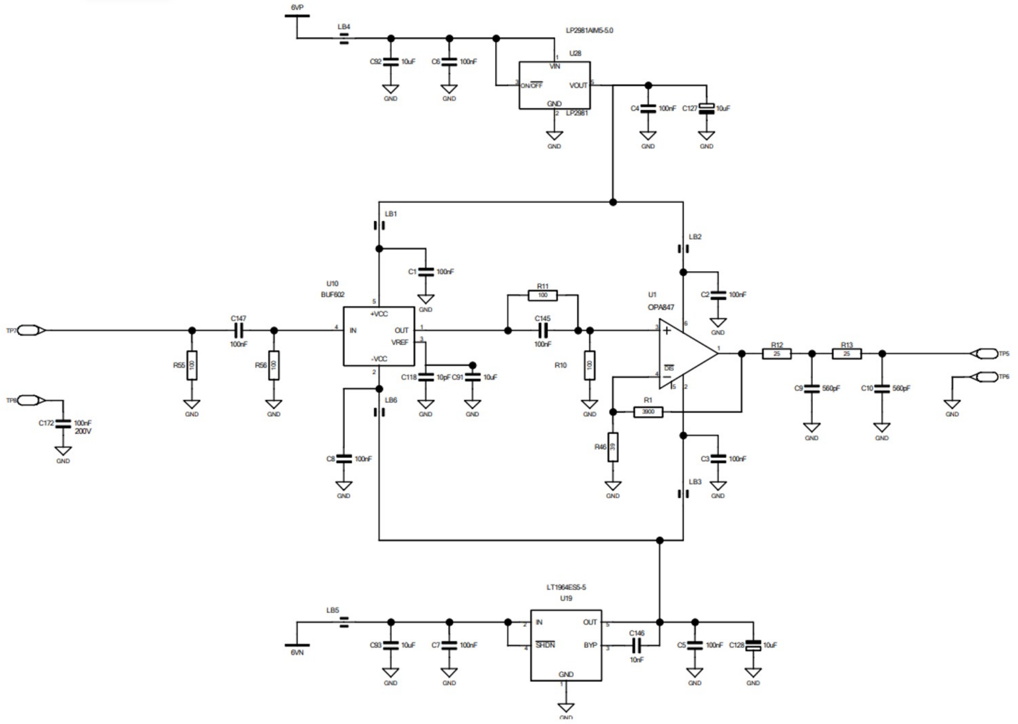

Figure 4.5: Circuit diagram of the Prototype 2 readout system configuration with a BUF602 buffer and one non-inverting OPA847 amplifier.

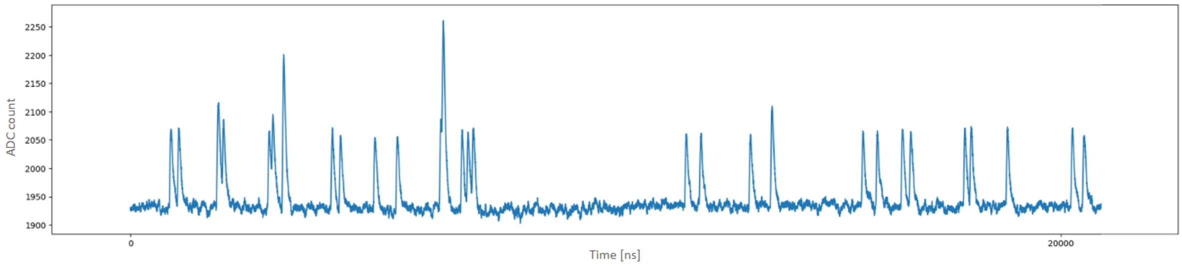

Figure 4.6: SiPM signal trace taken at VULCAN with the Prototype 2 readout system configuration showing improved SNR and a more unstable compared to Prototype 1.

4.2.3 Prototype 3

The third prototype follows a similar design to Prototype 2 but with the buffer removed. By doing this, the OPA847 amplifier becomes the first component in the signal path. This adjustment is intended to reduce the output noise since the input voltage noise of the amplifier is around 5 times lower than that of the buffer. Removing this component allows for signal amplification without the noise introduced by the buffer. It had to be ensured that this did not lead to oscillations or instabilities as observed in Prototype 1. With the buffer gone, a 50Ω shunt resistor was implemented as the current-to-voltage converter. Additionally, the gain was reduced from 100 to about 80. This was done to shift the baseline of the signal output closer to 0V.

The configuration for Prototype 3 is essentially equivalent to Prototype 2, but it exploits the low noise properties of the amplifier while simplifying the overall circuit design. A circuit diagram for Prototype 3 is shown in figure 4.7. Initially, the signal that was captured with this setup had a very low SNR. After several tests it was concluded that part of the noise originated from the SiPM bias power supply, and part from to the lack of proper grounding of the vacuum chamber. Figure 4.8 shows a dark count signal trace that was captured using the Prototype 3 configuration after tackling these issues.

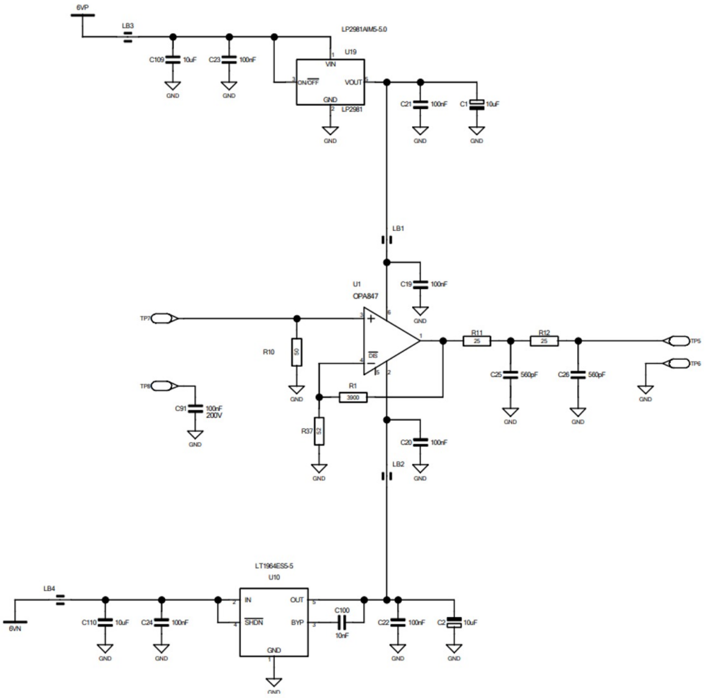

Figure 4.7: Circuit diagram of the Prototype 3 readout system configuration without a buffer and one non-inverting OPA847 amplifier.

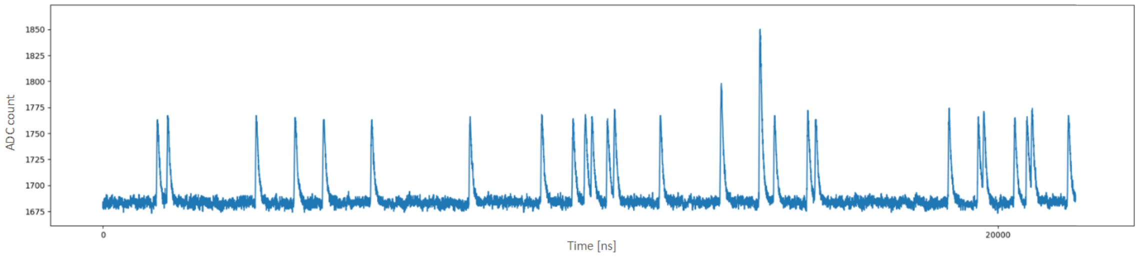

Figure 4.8: SiPM signal trace taken at VULCAN with the Prototype 3 readout system configuration showing a less noisy baseline compared to Prototype 2.

4.2.4 Prototype 4

The fourth prototype uses a transimpedence amplifier (TIA) instead of the non-inverting amplifier used in the previous designs. A TIA is a commonly used amplifier for SiPM signal processing. It directly converts the current output into a voltage signal by using a feedback resistor. In the other prototypes, increasing the resistance to get more gain also increases the input impedance. This input impedance forms a barrier that prevents the signal from passing through the amplifier. This does not happen with the TIA where the input impedance remains very low (nearly 0Ω) regardless of the resistance of the feedback resistor. This makes it possible to achieve a bigger gain without significantly affecting the input impedance.

Figure 4.9 shows a simplified TIA circuit with a feedback loop from the output of the operational amplifier (Op-Amp) back to the inverting input, which is how the TIA converts current into voltage. The SiPM is connected to the inverting input of the Op-Amp and the non-inverting input is grounded. Because the Op-Amp keeps the voltage difference between the inputs around zero, the inverting input is also set to the ground value. The current generated by the SiPM flows into the inverting input. Due to the low input impedance the current cannot flow through the Op-Amp and flows through the feedback resistor. This generates a voltage which becomes the output voltage of the amplifier.

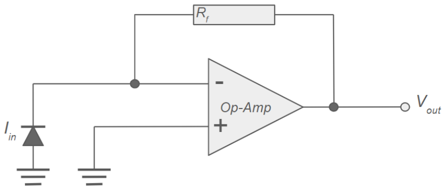

Figure 4.9: Simplified transimpedence amplifier circuit.

Figure 4.10 shows the circuit diagram of Prototype 4 where the TIA is incorporated. This configuration offers a more efficient method for current-tot-voltage conversion. This translates to a higher peak amplitude of the SiPM signal and the best SNR achieved so far. The improvement is visible in Figure 4.11, which shows a dark count signal trace captured using the Prototype 4 setup. Unfortunately this configuration is more sensitive to imperfections in the layout, improper grounding and parasitic effects. It requires a more careful and detailed design to achieve stability. During the testing phase these sensitivities led to inconsistent behavior in the prototype, highlighting the need for further improvements in the design.

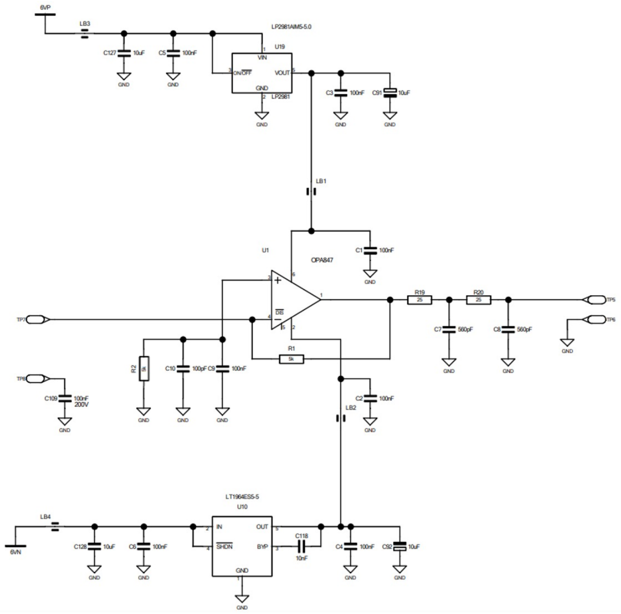

Figure 4.10: Circuit diagram of the Prototype 4 readout system configuration with a transimpedence amplifier.

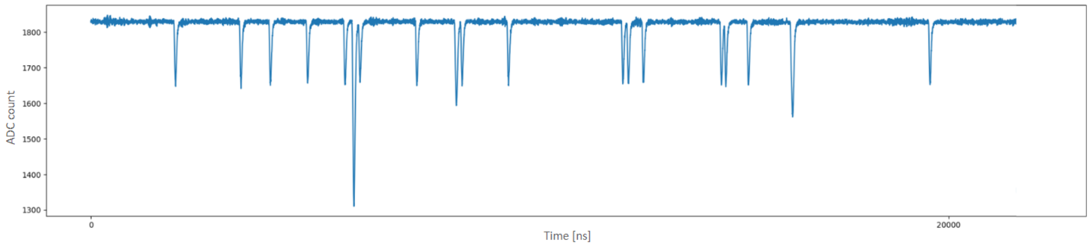

Figure 4.11: SiPM dark count signal trace taken at VULCAN with the Prototype 4 readout system configuration showing the highest SNR and most stable baseline compared to the other prototypes. The signal is inverted due to the use of a TIA.

4.3 Final Readout System

After the failure of the readout channels in Prototype 1, three new prototypes were developed. The oscillations and instabilities that occurred in Prototype 1 were not observed in Prototype 2-4. This can be attributed to their higher gain which reduces the bandwidth and blocks the high-frequency noise from entering system. The Prototypes 2-4 all performed well enough to analyze the SiPM signal. Prototype 4 showed the highest peak amplitude and SNR but proved to be unstable over time. The final readout system that was used for this project was based on Prototype 3, which offered the second best SNR and demonstrated consistent stability.

Figure 4.12 shows how a printed circuit board (PCB) with three Prototype 3 configuration channels is placed inside the aluminium readout box casing. Both the PCB and the readout box are designer to accommodate up to nine channels. The three channels that are currently installed are connected to the three SiPMs in the vacuum chamber via the D-sub connector. The blue holes on top of the readout box contain screws to manually adjust the bias voltage to the SiPMs individually. The coaxial cables on the side of the box are connecting the readout system to the input channels of the digitizer.

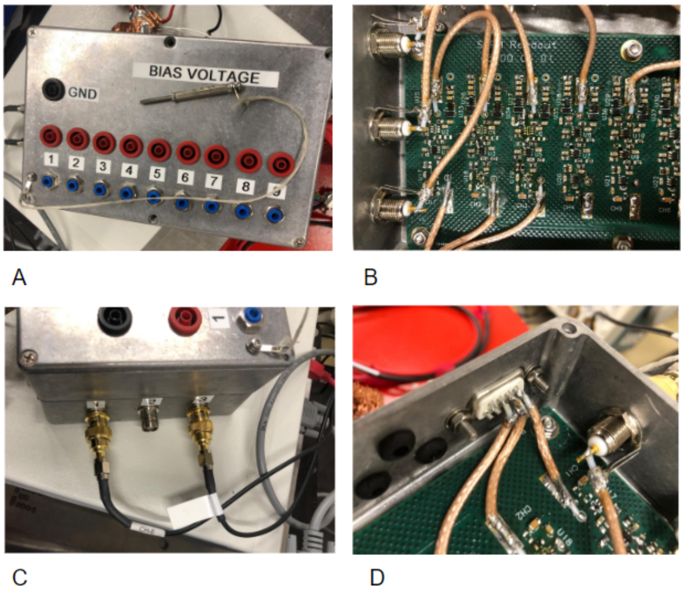

Figure 4.12: (a) Closed readout box with openings to manually adjust and measure the V_{BIAS}. (b) PCB with three Prototype 3 configurations inside the box. (c) Coaxial cables connecting the readout system to the digitizer. In this photograph only channel 1 and 3 are connected. (d) The three Prototype 3 configurations are connected to the SiPMs a D-sub connection.

5

Preliminary Calculations and Characterization

5.1 Data Analysis

5.1.1 Appending Digitizer Data

The SiPM signal is analyzed by calculating the light intensity. For each measurement run, data is collected by the digitizer for approximately 30 seconds, the maximum amount of data that can be written to the lab computer without processing issues. The data is taken in 30140 ns "snippets" at a frequency of 500 MHz. This digitized data is then read in and plotted using Python3. Figure 5.1 shows one snippet of raw data for the three SiPM channels. At the end of each snippet the data drops to zero. If we visualize our data for a longer period it looks like Figure 5.2.

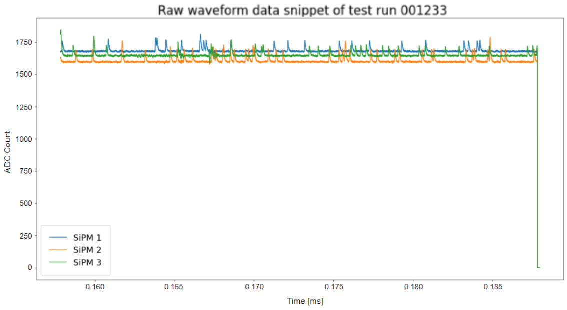

Figure 5.1: A single raw data snippet of 30240 ns.

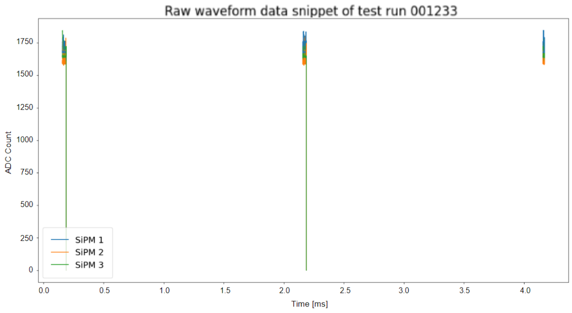

Figure 5.2: Visualization of multiple data snippets.

The first step in the analysis involves appending the data snippets. This does not affect the results, as the snippets represent continuous segments of the SiPM signal. Because the snippets are collected at a consistent sampling rate, the appended data preserves the integrity of the signal. The sampling rate is high enough to ensure that changes in signal intensity are captured. By appending the data snippets shown in Figure 5.2, a continuous waveform is created that is shown in Figure 5.3. This approach makes it easier to analyze the measurement runs.

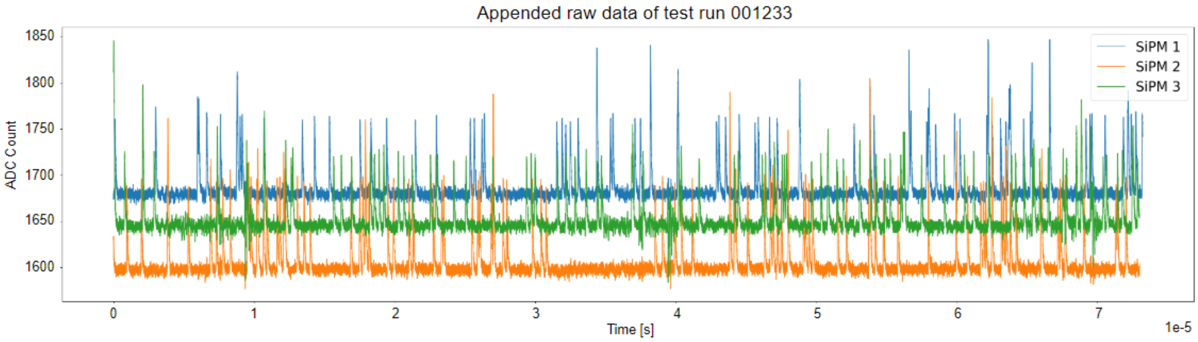

Figure 5.3: The data from Figure 5.2 appended to create a continuous data signal trace.

5.1.2 Calculating Light Intensity

To calculate the light intensity, it is necessary to determine the number of photons per second. Directly counting the amount of photon peaks within a time interval is not possible due to peak overlap. Instead, the total area under all the peaks is calculated and divided by the area of a single PE peak. This gives the total amount of 1 PE peaks which will be devided by the time to calculate the intensity. This is done by plotting the baseline in our signal and identifying all the signal peaks. The points where the peaks intersect the baseline are taken as the peak boundaries. The area within these peak boundaries is integrated. As shown in Figure 5.4 there are single peaks and peaks that overlap or are stacked on top of each other. Since this signal trace shows dark count signal, it can be assumed that the single peaks are the 1 PE peaks. The area of the overlapping peaks represent higher-order peaks like 2 PE, 3 PE and so on.

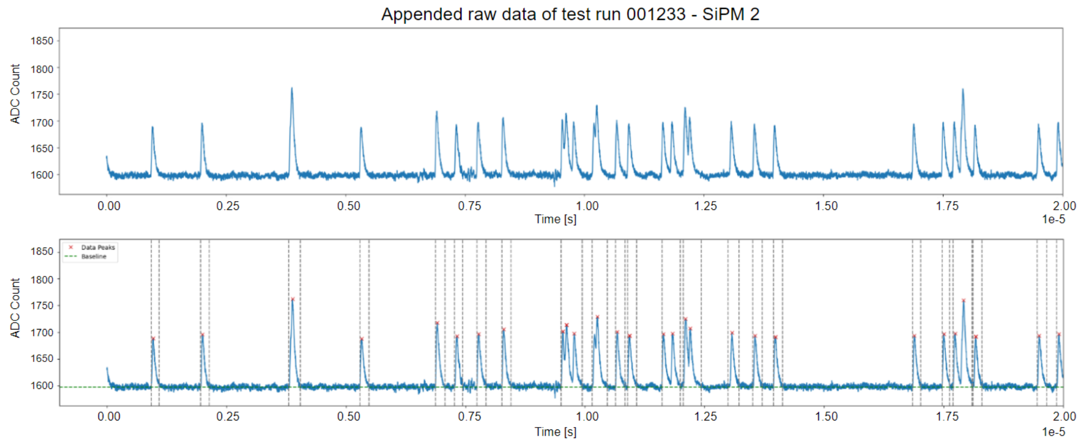

Figure 5.4: The trace on top shows the raw dark count signal. In the trace below, the red crosses indicate the signal peaks and the vertical dashed lines indicate the integration boundaries.

Creating a histogram with all the integration areas reveals the distinct peak sizes corresponding to the different order PE peaks. The distance between these peak sizes is the area of a 1 PE peak, also referred to as the gain. This distance is determined by plotting a multi-Gaussian fit with a constant spacing. By dividing the total integrated area by the gain and the time, the amount of 1 PE signal peaks per second can be calculated. This method is summarized by the formula:

$$\text{1 PE count rate} = \frac{\frac{\text{Total peak area}}{\text{Gain}}}{\text{Time}} \tag{5.1}$$

Because the gain is dependent on a lot of factors such as the temperature, the SiPM bias voltage and the amplification bias voltage, it needs to be calculated for each measurement.

The 1 PE rate that is calculated using this method includes both photon signal peaks and dark count signal peaks. To determine the true light intensity, the dark count signal must be subtracted. This is done by conducting a separate measurement without light. The dark count rate is calculated using the same method, and subtracted from the 1 PE rate from the light measurement. Because the SiPM dark count is not constant and depends on temperature and bias voltage, it must be repeated before every intensity measurement. The true light intensity is thus calculated by the formula:

$$\text{Light intensity} = \text{1 PE count rate} - \text{Dark count rate} \tag{5.2}$$

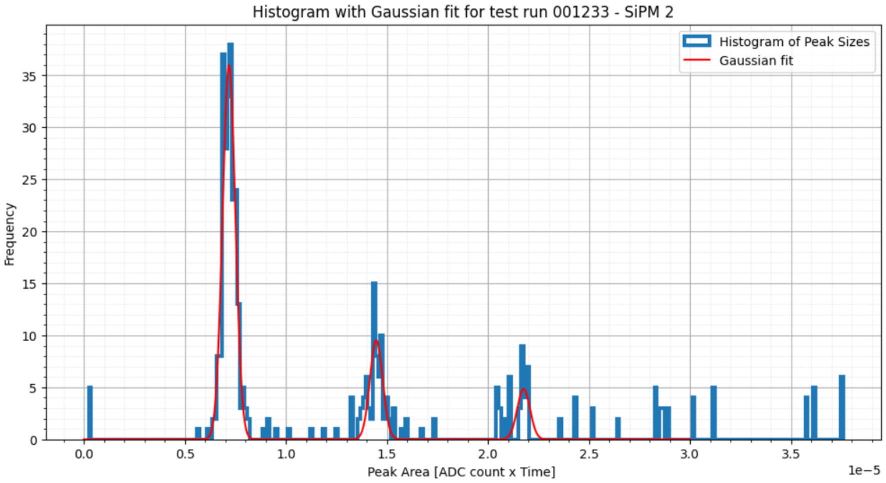

Figure 5.5: Histogram of the peak areas from one measurement run showing distinct peaks corresponding to the 1 PE, 2 PE and 3 PE signal peaks. The 2 PE and 3 PE peaks are formed by overlapping or stacked signal. The distance between the peaks in the histogram represents the gain.

5.2 Determining V_{BD} and V_{OP}

In order to perform a light intensity measurement, the SiPMs need to be biased at their operating voltage bias V_{OP}. The optimal operating voltage of the VUV-MPPC S13370-3050CN SiPMs is set 4 V above the breakdown volatage V_{BD} (26). The V_{BD} for each SiPM is determined by applying different bias voltages and calculating the gain from the dark count signal. The V_{BD} is the voltage at which the gain drops to zero. The results are shown in Figure 5.6.

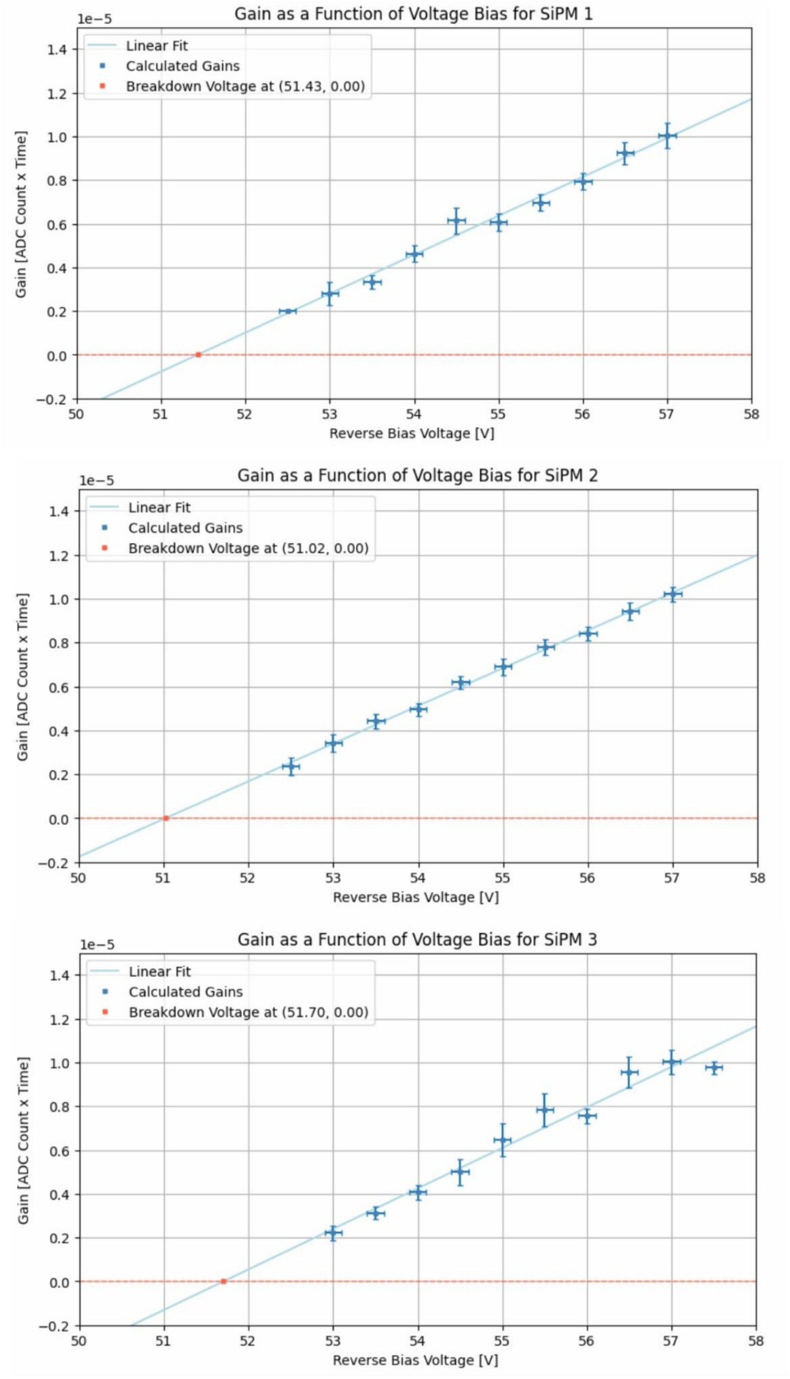

Figure 5.6: Determination of the V_{BD} for the three SiPMs in the VUV setup. The intersection point marks the threshold voltage that is necessary for the SiPM to operate. The V_{OP} is calculated as the V_{BD} + 4 V.

5.3 Reflection Standard Calibration

In order to calculate the reflectivity of material samples, a reflection standard with known reflectivity must be used. During this project the Thorlabs PFSQ20-03-F01 UV-Enhanced Aluminium mirror with known reflectivity over the 220 nm - 450 nm wavelength range is used as reflection standard. By comparing the intensity of the light reflected by the standard to the light reflected by our sample, the reflectivity of the sample can be calculated. The VUV setup is aligned by placing the sample holder at approximately a 45 degree angle and rotating the sensor holder to detect the highest light intensity on the center SiPM using an oscilloscope. Measurement runs are taken over a range of angles around this position to catch all the reflected light because this method of alignment is not exact and the ligth is not perfectly specular. The sample holder is then rotated 180 degrees to repeat the measurement for the sample.

The primary wavelength of interest for this project is the 128 nm wavelength which is the scintillation wavelength of LAr. Reflectivity at 175 nm, the scintillation wavelength of xenon used in dark matter detectors, is also measured. The challenge is that the reflection standard provides data only for wavelengths down to 220 nm light. It is necessary to first determine the reflectivity of the standard for the wavelengths of interest which are below 220. This is done by measuring the reflected light intensity of the standard for all wavelengths of interest along with two reference wavelengths for which the reflectivity data is provided. The results of these measurements are presented in Figure 5.7.

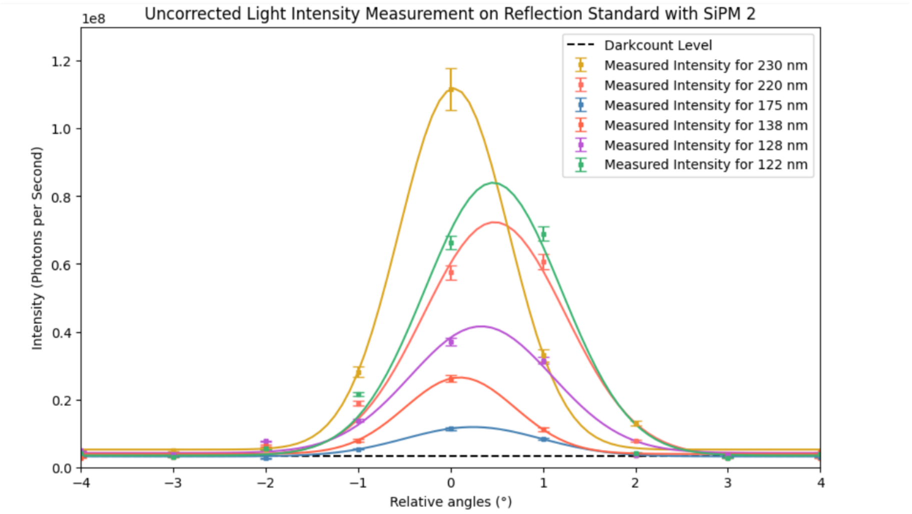

Figure 5.7: Uncorrected intensity measurements of the light reflected by the reflection standard across various wavelengths of interest and reference wavelengths.

Calculating the reflectivity at the lower wavelengths by taking the reference wavelengths and use the ratios is not possible due to necessary wavelength corrections. Figure 5.6 presents the uncorrected light intensity measurements. The Deuterium lamp emits light at varying intensities, the monochromator grating reflects light with different efficiencies, and the SiPM shows varying sensitivity across different wavelengths of light. The spectral data that is provided by the suppliers is plotted in Figure 5.5. In order to accurately calculate the reflectivity of the reflection standard at lower wavelengths, the measured light must be corrected for these components in the experimental setup.

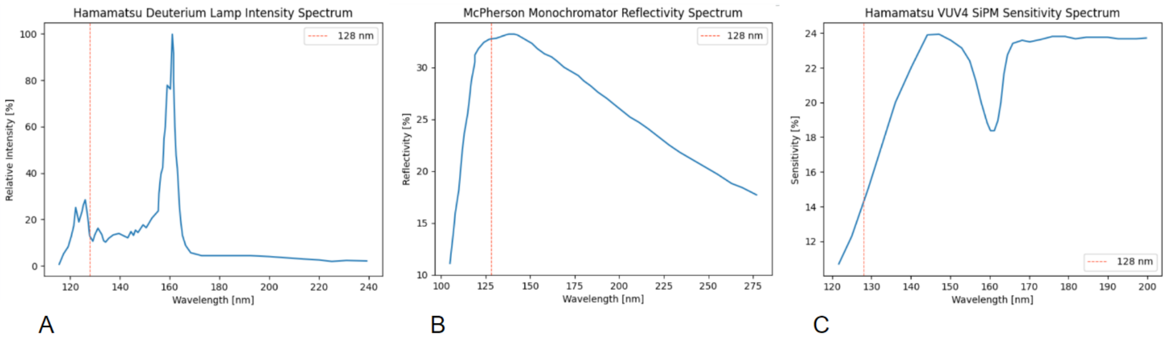

Figure 5.8: (a) Spectrum of the Hamamatsu deuterium lamp. (b) Efficiency of the McPherson Monochromator grating in reflecting various wavelengths of light. (c) Sensitivity of the Hamamatsu VUV4 SiPMs for different wavelengths of light. The dashed red lines indicate 128 nm which is the wavelength of liquid argon scintillation light.

Figure 5.9 shows the light intensity peaks from Figure 5.6 together with the expected intensity when the correction factors are taken into account, assumed that the standard reflects the same for every wavelength. These corrections are normalized to 230 nm for which the reflectivity of the standard is known. By taking the ratio between the expected intensity and the measured intensity, the reflectivity of the reflection standard at specific wavelengths can be determined. The results of this calculation are provided in Figure 5.10. With the reflectivity of the reflection standard established across all wavelengths of interest, it can now be used as a reference for the sample measurements.

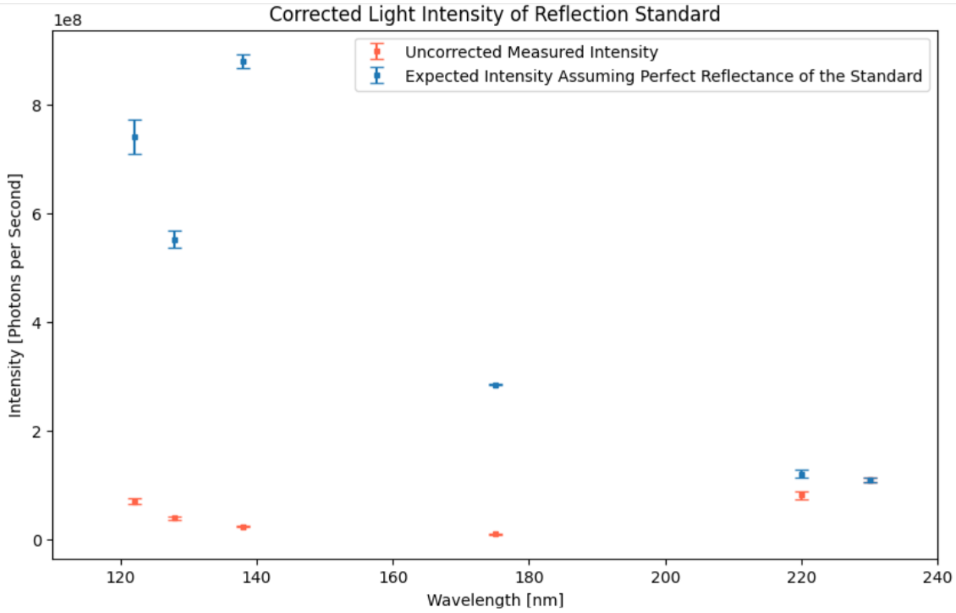

Figure 5.9: Corrected light intensity plot for the reflection standard. The orange points represent the peak intensities from the uncorrected reflected light intensity measurements. The blue points indicate the corrected intensities, normalized at 230 nm and assuming that the standard reflects the same across all wavelengths.

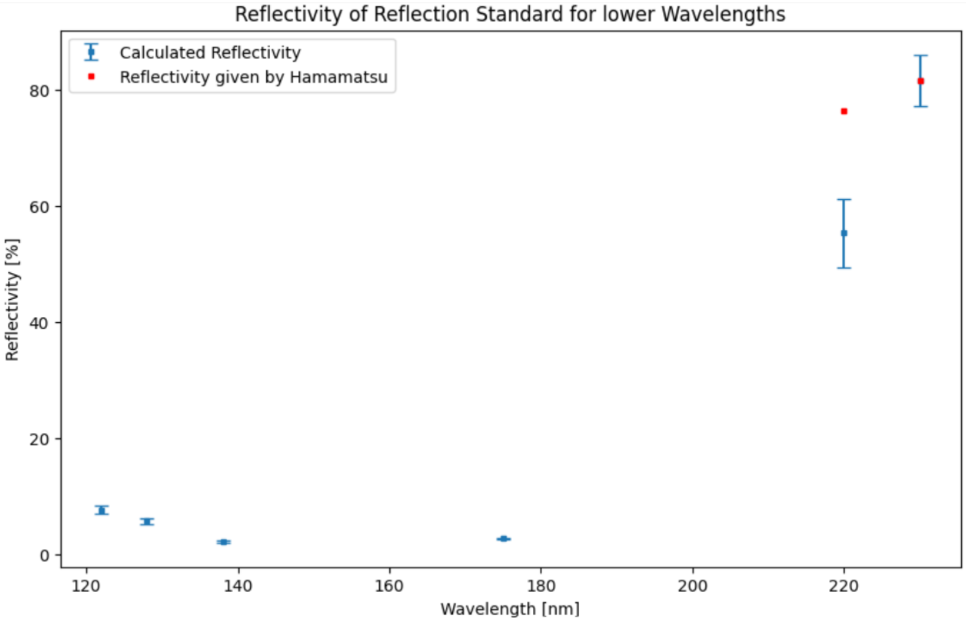

Figure 5.10: Reflectivity of the reflection standard for wavelengths below 220 nm. The blue points represent the calculated reflectivity for all wavelengths of interest. The red points indicate the reflectivity for the standard provided by Hamamatsu.

5.4 Spot Size Estimation

The light intensity calculation methods and results presented in the previous chapter are shown for only one SiPM, the center SiPM (SiPM2). For the final analysis, these calculations will be repeated for all three SiPMs separately, rather than combining their signals. This is necessary because the spot size of the light beam was not precisely determined, which makes it impossible to quantify how much light falls on each SiPM.

Figure 5.11 shows the technical drawing of the S13370-3050CN SiPM. Each SiPM has a 3.0×3.0 mm active area and a 1.45 ± 0.08 mm dead region on the left and right side. Figure 5.12 shows how light is distributed over two adjacent SiPMs during an intensity measurement. When one SiPM is perfectly aligned with the reflected beam, the other one does not receive light. This observation suggests that the beam spot is no wider than the combined width of one SiPM (5.9 ± 0.15 mm) and the dead regions of the adjacent SiPMs (2.9 ± 0.15 mm), resulting in a total maximum width of 8.8 ± 0.30 mm.

Figure 5.12 also shows areas of overlap where one SiPM receives approximately half of its maximum light intensity while the other receives about one-third. A rough estimate of the beam spot size can be calculated as the width of half of the active area (1.5 mm) plus one-third of the active area (1.0 mm) plus the dead region between them (2.9 ± 0.15 mm). This leads to an estimated total width of approximately 5.4 mm, which is within the width of a single SiPM. This remains a rough estimate and it lacks the precision that is necessary to combine the light collected by all three SiPMs. It also does not account for the effect of diffusive reflection. Even though the reflection standard should be relatively smooth, the reflection is not perfectly sepcular. Therefore, each SiPM is analyzed separately, with results combined at the end of the analysis.

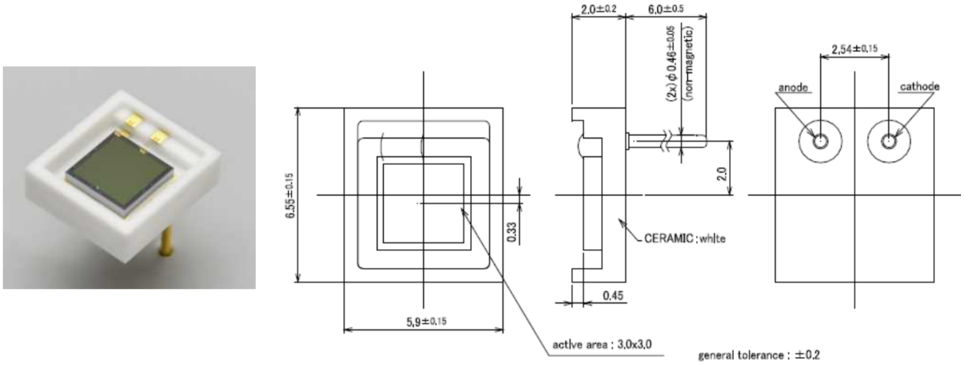

Figure 5.11: Technical drawing of the VUV-MPPC (VUV4) S13370-3050CN SiPM provided by Hamamatsu. (26)

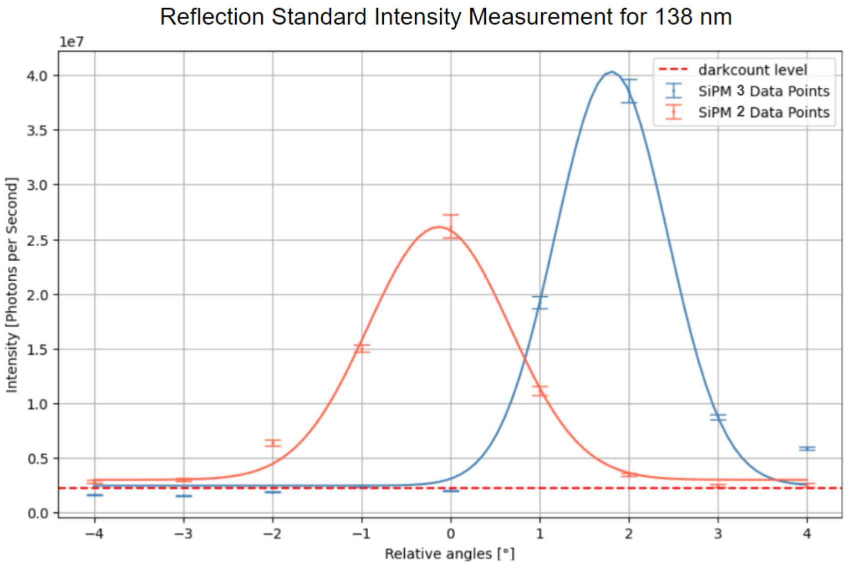

Figure 5.12: Results from a single reflected light intensity measurement for two adjacent SiPMs in the VUV setup. At the peak light intensity of one SiPM, the adjacent SiPM receives no light, indicating that there is no light overlap at the point of perfect alignment. The degree of overlap at angles between perfect alignment suggests that the spot size of the light beam is smaller then the width of one SiPM.

5.5 VUV Light Absorption

5.5.1 Establishing the Vacuum

Since all wavelengths of interest for this projects are within the VUV range, a sufficient vacuum needs to be established to prevent light absorbtion by air. The Pfeiffer Vacuum HiCube 80 Eco DN63 can achieve an ultimate pressure of 1×10^{-7} mbar in a 10 L environment (37). The lowest pressure achieved at the start of the project was 1.6×10^{-3} mbar after a full day of pumping, indicating that there was a leak in the setup. After ruling out leaks in the pump and in the monochromator-lamp stage by directly connecting the pressure to the monochromator, it was concluded that the leak was in the vacuum chamber. A helium leak test revealed multiple leaks around the plates of the chamber which suggested that the sealing was faulty. Replacing the O-rings with new, clean O-rings did not solve the issue. Further inspection led to the conclusion that the O-rings supplied by Ideal Vacuum with a diameter of 3.7 mm were too thin and flattened between the frame and the plates of the vacuum chamber. New O-rings with a diameter of 4 mm were ordered from Seal Supply. After replacing the Ideal Vacuum O-rings with the Seal Supply O-rings, a vacuum of 7.4×10^{-5} mbar was achieved within a few hours.

5.5.2 Light Path Calculation

In order to calculate the light absorption in air, the length of the light path from the point of emission to the SiPM has to be determined. The light travels 110 ± 4 mm through the deuterium lamp, followed by 381 mm through the monochromator(33)(36). The light path within the vacuum chamber varies depending on the positions of the sample holder and the SiPM holder. Our sample is angled at nearly 45 degrees with respect to the light beam. This alignment done visually so there is no way to know the exact angle. Figure 5.13 shows the configuration for a 40° and a 45° angle and their corresponding light path lengths. Since the precise angle is unknown and likely falls within this range, the path length inside the chamber is estimated at 150 mm. Therefore, the total light path length is calculated as $150 + 110 + 181 = 641$ mm, or approximatetely 64 cm.

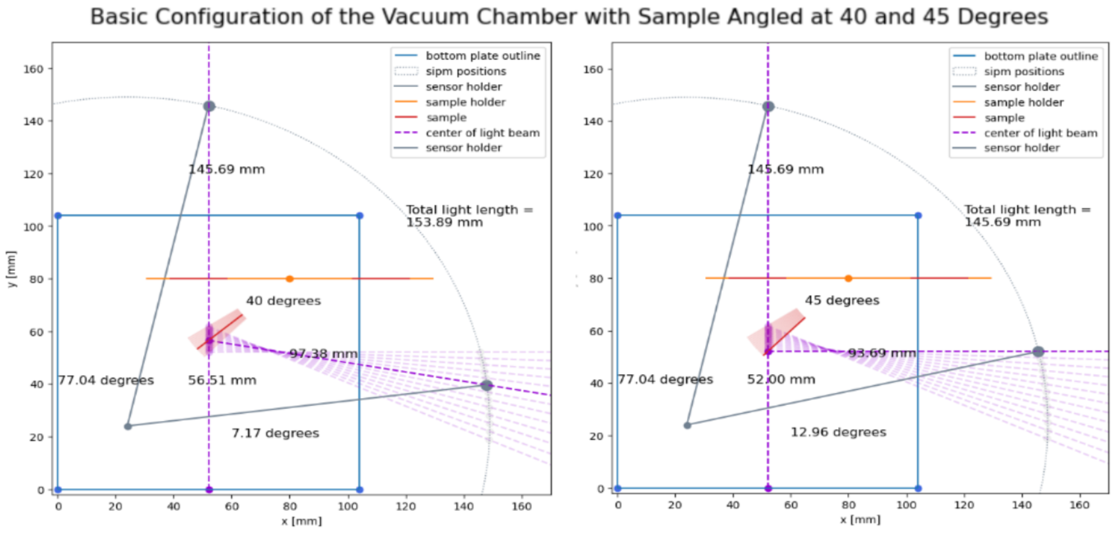

Figure 5.13: Vacuum chamber configuration for a 40° and 45° angle of the sample holder with respect to the light beam. The total length of the light path in the chamber is given in the figure. The code used to plot these figures was written by Yannick Wishaupt.

5.5.3 Beer-Lambert-Bouguer Attenuation Law

The vacuum pressure that is required to prevent the VUV light from being absorbed can be calculated by the Beer-Lambert-Bouguer Law, as given in Equation 2.9. The light attenuation coefficient μ is expressed as:

$$\mu(P) = \rho(P) \cdot \frac{N_a \sigma}{M}. \tag{5.3}$$

Here, N_a is Avogadro's constant (6.02×10^{23} mol^{-1}), M the molar mass of oxygen, σ is the absorption cross section of the light, and ρ the pressure dependent density of oxygen in air, given by:

$$\rho(P) = P \cdot 0.2094 \times \frac{M}{RT}. \tag{5.4}$$

Here, T is the temperature, R is the gas constant (8.31 J $\cdot$ K$^{-1}\cdot$ mol^{-1}) and it is assumed that the oxygen concentration in air is 20.94%. Figure 5.14 presents the absorption cross sections for light in the VUV range, highlighting the wavelengths of interest for this project. For LAr scintillation light the absorption cross section is set at 10^{-22} m^2. Substituting equation 5.4 into equation 5.3 and filling in the values gives:

$$\mu(P) = P \cdot \frac{0.2094 \times 6.02 \times 10^{23} \cdot 1 \times 10^{-22}}{8.31 \times 297} = 0.0051 \times P. \tag{5.5}$$

By taking Equation 5.6 and the calculated path length, the light attenuation equation (Equation 2.9) for LAr scintillation light in the VUV setup can be written as:

$$\frac{I}{I_0} = e^{-0.0051 \times P \times 64} = e^{-0.3264 \times P}. \tag{5.6}$$

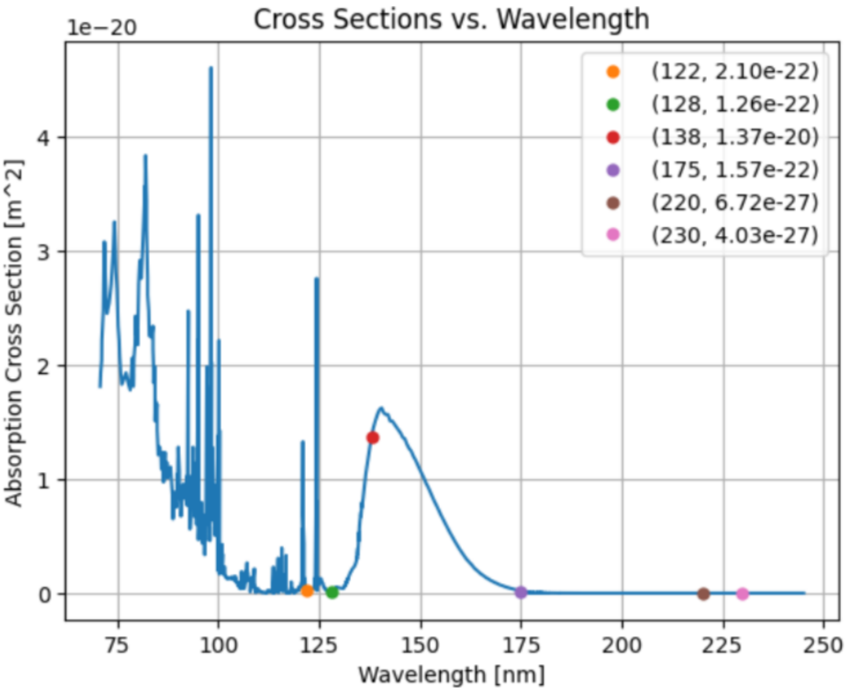

Figure 5.14: Absorption cross sections for wavelengths in the VUV range.

5.5.4 Vacuum requirements

For this experiment, a light intensity of at least 99.99% of the incoming light beam is desired. To meet this requirement, the following condition must be satisfied:

$$e^{-0.3264\times P} > 0.9999 \tag{5.7}$$

$$P < 0.00031 = 3.1 \times 10^{-4} \text{ mbar.} \tag{5.8}$$

For the reflection measurement at 128 nm, a vacuum of at least 3.1×10^{-4} mbar is required. The pressure during all measurements has been below 8×10^{-5} mbar. The achieved vacuum is sufficient for 99.99% light attenuation for wavelengths with a absorption cross section of 10^{-22} m^2 and below.

The 138 nm wavelength is the only wavelength of interest in this experiment with an absorption cross section larger then 10^{-22}. Filling in $\sigma = 10^{-20}$ (Figure 5.14) in equation 5.5 gives:

$$\mu(P) = 0.5108 \times P \tag{5.9}$$

$$\frac{I}{I_0} = e^{-0.5108\times P\times 64} = e^{-3269\times P}. \tag{5.10}$$

By substituting the pressure value of 8×10^{-5} mbar, the light attenuation is calculated as:

$$\frac{I}{I_0} = e^{-3269\times 8\times 10^{-5}} = 0.9974. \tag{5.11}$$

The light attenuation for 138 nm light in this setup is 99.74%, which translates to a light absorption of 00.16%. This effect is minimal and negligible when compared to the measurement uncertainty

5.6 Pressure Dependency

During the reflectivity measurements a certain pressure needs to be maintained, meaning that the vacuum pump needs to pump continuously to uphold this pressure. The continuous pumping may lead to fluctuations in pressure that can influence the VUV light attenuation following Equation 2.9. To minimize this, the measurements were started after an extended period of pumping to reach stable pressure conditions. To determine the impact, pressure data from inside the vacuum chamber was collected over periods of 3.5 hours, which is the approximate duration of a complete measurement. One of these measurements is shown Figure 5.15. The pressure variations during the measurement were substituted into Equation 5.10, where the effect on light attenuation is biggest due to the larger cross section. The effect on light attenuation is 0.0105%. This is negligible when compared to the overall measurement uncertainty and does not affect the experiment's results.

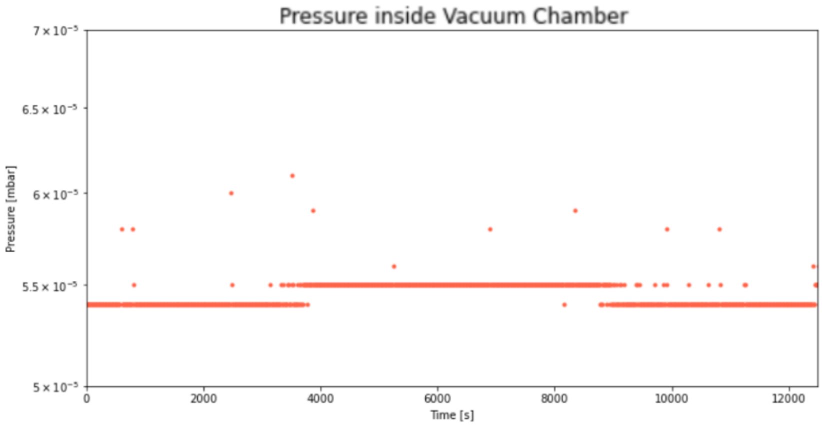

Figure 5.15: Pressure data from inside the vacuum chamber during a single measurement.

5.7 Temperature Dependency

Temperature is variable that can have a significant impact on the measurement results. The temperature in the lab is not stable, and although the experiment is subjected to a vacuum, the temperature can be influenced by thermal conduction through the vacuum chamber walls. The main contributor to temperature variations is the deuterium lamp, that generates a lot of heat. Figure 5.16 shows the collected temperature data from inside the vacuum chamber for the duration of 3.5 hours, the duration of one reflectivity measurement. The temperature increase shows asymptotic behaviour. The heat generated by the lamp gets absorbed by the system, that over time approaches thermal equilibrium. Data shows that the total temperature increase during the measurements is less than 0.4 degrees kelvin.

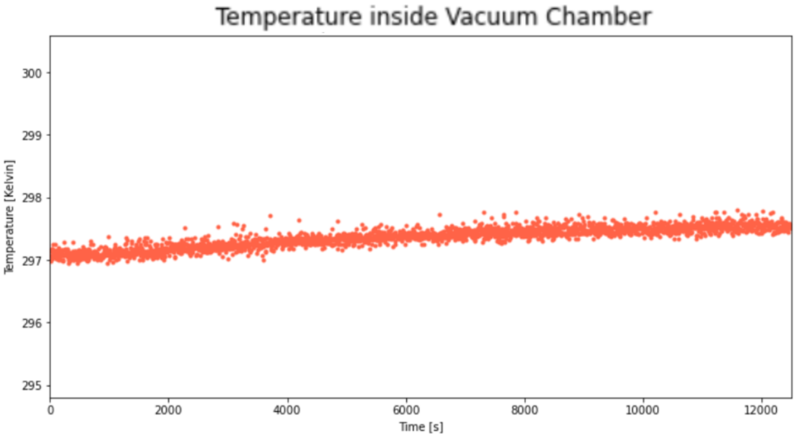

Figure 5.16: Temperature data collected from inside the vacuum chamber over the duration of one reflectivity measurement.

At room temperature and above, the dark count is strongly affected by temperature changes. Previous measurements conducted with VULCAN established the relationship between dark count and temperature for temperatures below room temperature. These results are shown in Figure 5.17. The original data from this measurement is no longer accessible but the relation could be re-visualized and extrapolated using the provided fit parameters, as shown in Figure 5.18. Assuming a temperature increase from 297 K to 297.5 K during the experiment, the dark count rate increases 2.52% according to this relation. This increase is small enough to be included in the overall uncertainty of the dark count rate. Since the details and errors from the original calculation are unknown, and the SiPMs might behave differently, an uncertainty of 3% is added to the overall dark count rate uncertainty.

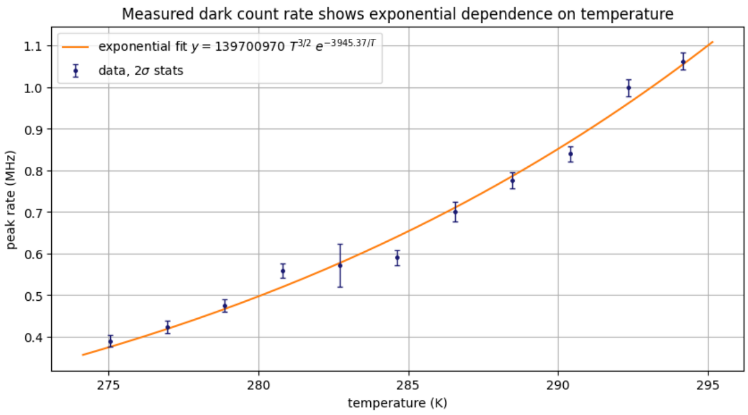

Figure 5.17: Relation between dark count rate and temperature established during previous project at VULCAN. (40)

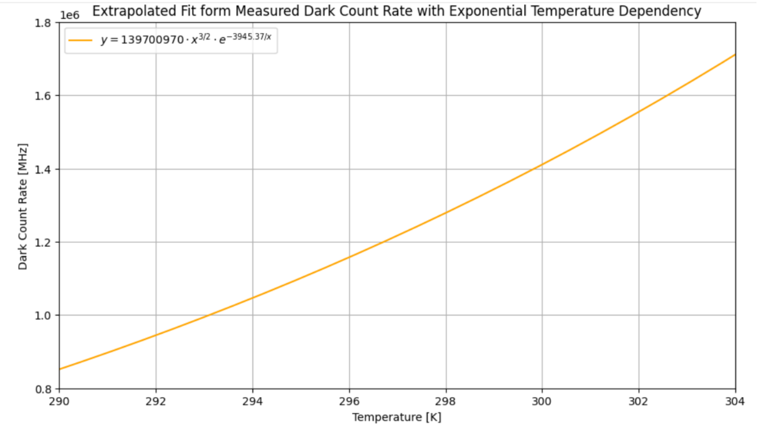

Figure 5.18: Relation between dark count rate and temperature re-visualized and extrapolated using the fit parameters from Figure 5.17.

6

Reflectivity Measurements

6.1 Reflection Standard

The wavelengths of interest are the wavelengths that are selected for the reflectivity measurements of the DUNE samples. They include 230 nm, 220 nm, 175 nm, 138 nm, 128 nm and 122 nm. The primarily focus is 128 nm which corresponds to the scintillation light of liquid argon. The two nearby wavelengths, 122 nm and 138 nm, are measured as a reference and to provide more insight. The scintillation wavelength of xenon used in dark matter detectors is 175 nm, which could be an interesting comparison point. The wavelengths of 230 nm and 220 nm serve as reference wavelengths since the reflectivity of the reflection standard is known at these wavelengths.

The method that is used to determine the reflectivity of the reflection standard for wavelengths below 220 nm is outlined in great detail in Section 5.3. The correction factors for the wavelengths of interest, obtained from the data plotted in Figure 5.8, are presented in the table in Figure 6.1. Figure 6.2 shows the uncorrected light intensity measurements for the reflection standard for all three SiPMs. After applying the correction factors, as described in Section 5.3, the reflectivity of the standard is calculated. The final results of this calculation are presented in Figure 6.3 and Table 6.1.

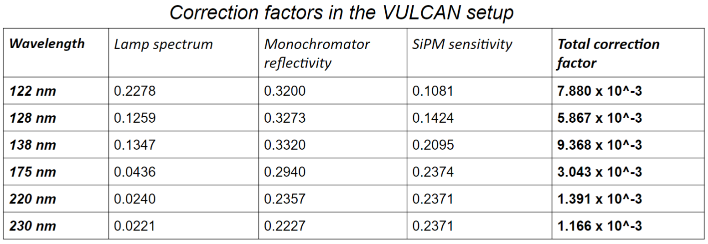

Correction factors in the VULCAN setup

Wavelength	*Lamp spectrum*	*Monochromator reflectivity*	*SiPM sensitivity*	***Total correction factor***
122 nm	0.2278	0.3200	0.1081	**7.880 x 10^-3**
128 nm	0.1259	0.3273	0.1424	**5.867 x 10^-3**
138 nm	0.1347	0.3320	0.2095	**9.368 x 10^-3**
175 nm	0.0436	0.2940	0.2374	**3.043 x 10^-3**
220 nm	0.0240	0.2357	0.2371	**1.391 x 10^-3**
230 nm	0.0221	0.2227	0.2371	**1.166 x 10^-3**

Figure 6.1: Correction factors of VULCAN components for wavelengths of interest.

6.1.1 Results

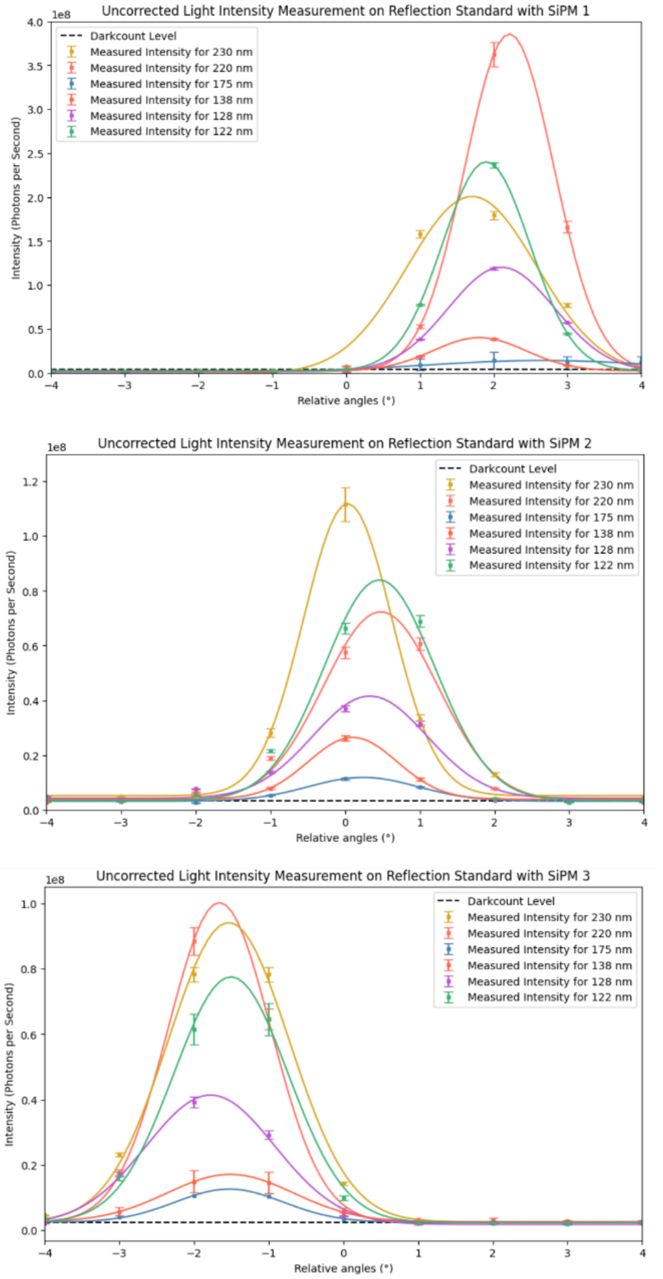

Figure 6.2: Uncorrected intensity measurements of the light reflected by the reflection standard at the wavelengths of interest. The results for SiPMs 1, 2 and 3 are presented from top to bottom. The three SiPMs show significant differences in light intensity. The error bars in this plot come from the statistical uncertainties, the uncertainties in the gain calculation, baseline calculation, the fit values and the dark count rate.

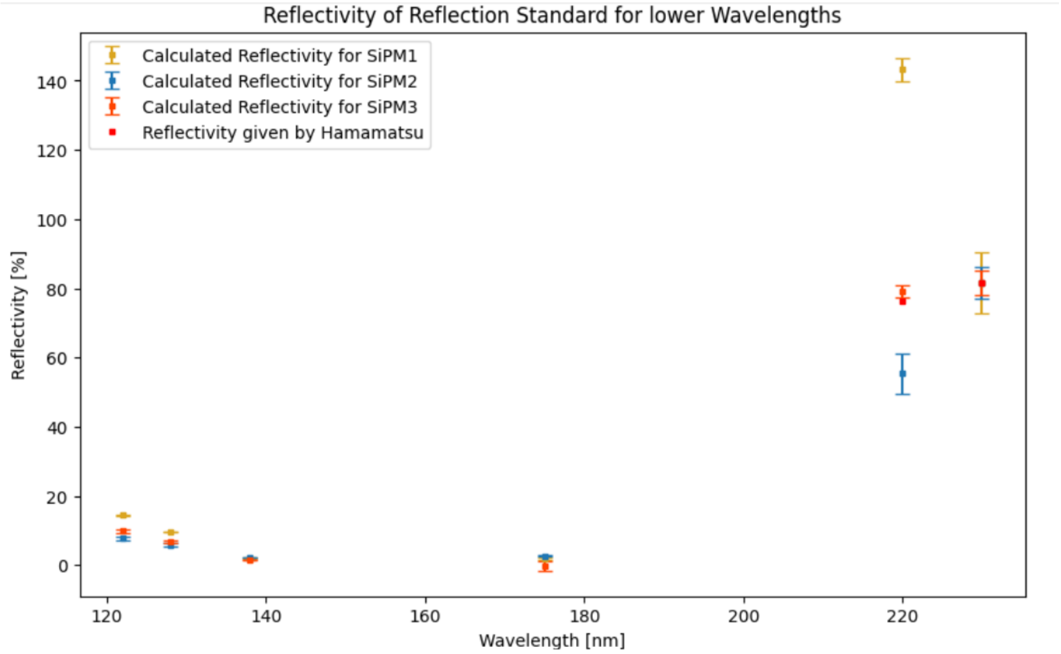

Figure 6.3: Reflectivity of the reflection standard calculated for the wavelengths of interest and normalized to 230 nm. The red points indicate the reflectivities of the standard provided by Hamamatsu. The error bars are the propagated uncertainties from Figure 6.2.

Reflection Standard Reflectivity

Wavelength	SiPM 1	SiPM 2	SiPM 3
122 nm	$14.5 \pm 0.2\%$	$7.7 \pm 0.6\%$	$9.9 \pm 0.5\%$
128 nm	$9.6 \pm 0.1\%$	$5.8 \pm 0.5\%$	$6.9 \pm 0.3\%$
138 nm	$1.9 \pm 0.1\%$	$2.2 \pm 0.1\%$	$1.6 \pm 0.1\%$
175 nm	$1.9 \pm 0.3\%$	$2.8 \pm 0.1\%$	$3.5 \pm 0.1\%$
220 nm	$143.2 \pm 3.4\%$	$55.3 \pm 5.9\%$	$79.1 \pm 1.8\%$
230 nm	$81.6 \pm 8.9\%$	$81.6 \pm 4.5\%$	$81.6 \pm 3.7\%$

Table 6.1: Reflectivity of the standard for wavelengths of interest. The values correspond to the data points shown in Figure 6.3.

6.1.2 Sources of Uncertainties

Several sources of uncertainty were considered in the calculations. First are Poisson uncertainties that are applied on the photon count rate. Next are the uncertainties in the gain calculation, which are derived from the peak widths in the PE histograms (Section 5.1.2.), and the uncertainties in the baseline calculation, determined by the noise level. The dark count rate is calculated with the same method that is used for intensity measurements, but an extra uncertainty is added due to temperature variations. Finally, uncertainties are also present in all fit variables. The data that is used for the correction factors did not provide any uncertainties, which might add to the discrepancies in the results.

6.1.3 Discussion

The results presented in Figure 6.3 show a significant decrease in reflectivity for wavelengths below 220 nm. This can be explained by the surface roughness of the aluminium reflection standard. Aluminium quickly oxidizes when it is exposed to air. The formation of the oxide layer creates irregularities on the surface which leads to surface roughness. As the wavelength decreases, the surface roughness becomes comparable in size to the wavelength itself. This leads to increased scattering and thus reduced reflected intensity. Another reason for lower reflectivity at shorter wavelengths is the absorption of the light into the oxide layer (41). Figure 6.4 present calculations by Stenzel et al., for oxide absorption in the VUV range.

A notable observation in the results is the unexpected increase in reflectivity for wavelengths below 138 nm. This behaviour is unusual, especially since an absorption band exists near 100 nm wavelength (42). Furthermore, the plasma frequency ω_p of aluminum corresponds to an energy of 15 eV (43). At wavelengths that correspond to the plasma frequency energy, electrons in the material resonate with the light. The material becomes transparent at this wavelength which leads to a strong decrease in reflectivity (44). A photon energy of 15 eV corresponds to a wavelength of 82.6 nm so it would be expected that the reflectivity decreases as the wavelength approaches 82 nm. Since there is no clear theoretical explanation for the increase in reflectivity in the results, it is possible that the observed trend is caused by inaccurate data and unknown uncertainties in the correction factors.

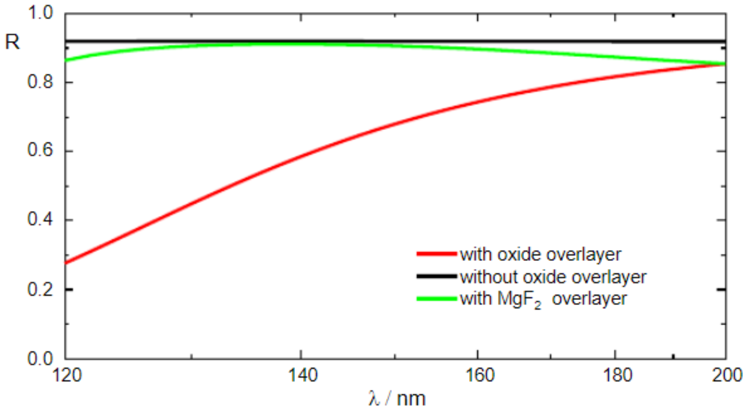

Figure 6.4: Calculated reflectivity of smooth aluminium surfaces. Aluminium with a smooth oxide layer still shows decreased reflectivity at lower wavelength which indicates that besides rough surfaces, absorption into the oxide layer also causes decrease in reflectivity. (41)

The results from the three SiPMs show notable discrepancies. Figure 6.3 indicates that the result from SiPM 3 is the most accurate because it aligns best with the provided reflectivity at 220 nm. This conclusion should be taken with caution because Hamamatsu has stated that for the lower wavelengths the provided reflectivity may not be accurate. This could also mean that the measurement may have been normalized to a faulty value. The reflectivity at 220 nm measured with SiPM 2 deviates from the reference value by over 25%. We can not say anything about the quality of this measurement due to the absence of uncertainties in the data provided by Hamamatsu. The reflectivity for the lower wavelengths calculated with SiPM 2 and SiPM 3 seem to correspond quite well.

The results for SiPM 1, however, seem to be unreliable. This can be attributed to the configuration of the vacuum sample chamber. During the measurements the sample holder is rotated over a range of angles to capture the light while the SiPMs remain stationary. This rotation changes the angle of incidence on the SiPMs which might affect light capture. SiPM 1 is positioned the furthest to the right in the sensor holder in Figure 3.4 and is affected the most by this geometrical issue, which could explain the results from section 6.1.1. The angle of incidence of the reflected beam is most perpendicular to SiPM 3. Therefore, the results from SiPM 3 will serve as the reference for the reflectivity measurements.

6.2 DUNE Samples

With the reflectivity of the reflection standard established for all wavelengths of interest, it can be used as a standard to calibrate the reflectivity measurements on the DUNE samples. This is done by conducting the measurements on the sample and then rotating the sample holder to conduct one measurement on the reflection standard at one of the wavelengths of interest, the reference wavelength. The reflectivity of the sample at the reference wavelength can be directly calculated by taking the ratio of the sample's measured intensity to the standard's intensity because there is no wavelength correction needed. For the other wavelengths the correction factors need to be applied. Instead of reapplying the correction factors for each measurement, the ratios between the measured intensities from the standard calibration measurement in Section 6.1 are used. For each sample measurement at a specific wavelength, the ratio between that wavelength and the reference wavelength is extracted from the intensity plots of the standard (Figure 6.3). The formula used to calculate the reflectivity of a sample at a given wavelength is:

$$\text{Sample Reflectivity}_\lambda = \frac{\text{Intensity}_\lambda \cdot \text{Standard Reflectivity}_\lambda}{\left(\frac{\text{Calibration Measurement Intensity}_\lambda}{\text{Calibration Measurement Intensity}_{Ref}}\right) \cdot \text{Intensity}_{Ref}}. \tag{6.1}$$

The uncertainties mentioned in Section 6.1 are all propagated through this calculation.

Section 6.2.1 presents the results of the reflectivity measurements for the DUNE detector samples. Prior to being placed in the VUV setup, the samples undergo ultrasonic cleaning to remove contaminants from the surface.

6.2.1 Results

6.2.1.1 Al PCB

The first sample is a piece of aluminium from a printed circuit board made at the Instituto de Física Corpuscular (IFIC), located at the University of Valencia. A photograph of this sample is shown in Figure 6.5. The results of the intensity measurements for this sample are shown in Figure 6.6. The corresponding reflectivities, calculated using Equation 6.1, are presented in Figure 6.7 and Table 6.2.

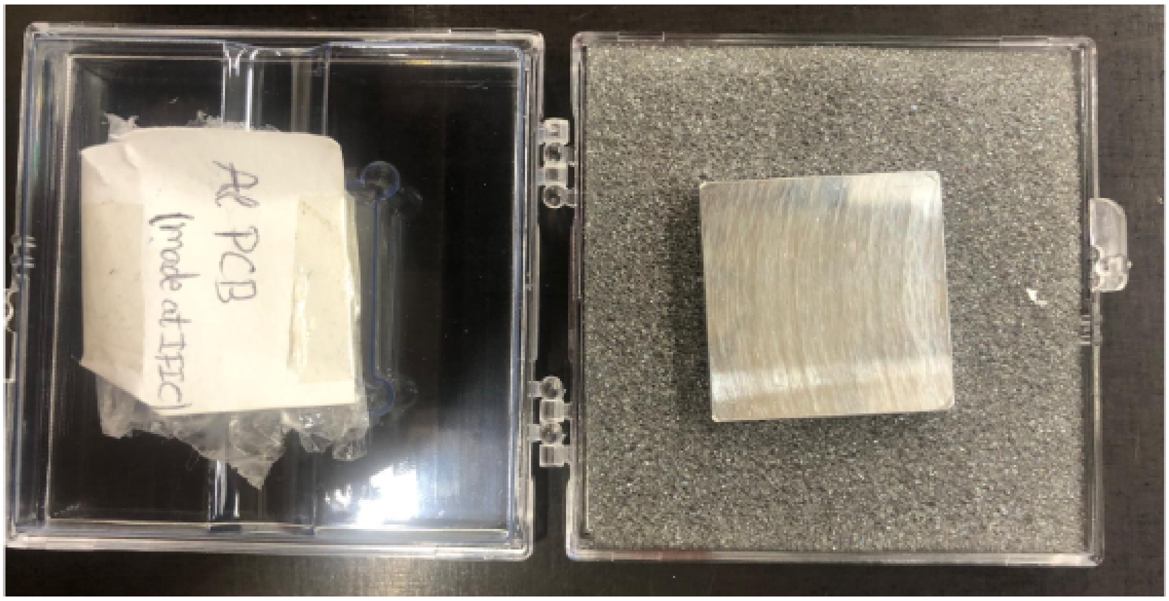

Figure 6.5: Photograph of the first sample used for reflectivity measurements. It is a piece of aluminum from a printed circuit board manufactured at the Instituto de Física Corpuscular (IFIC).

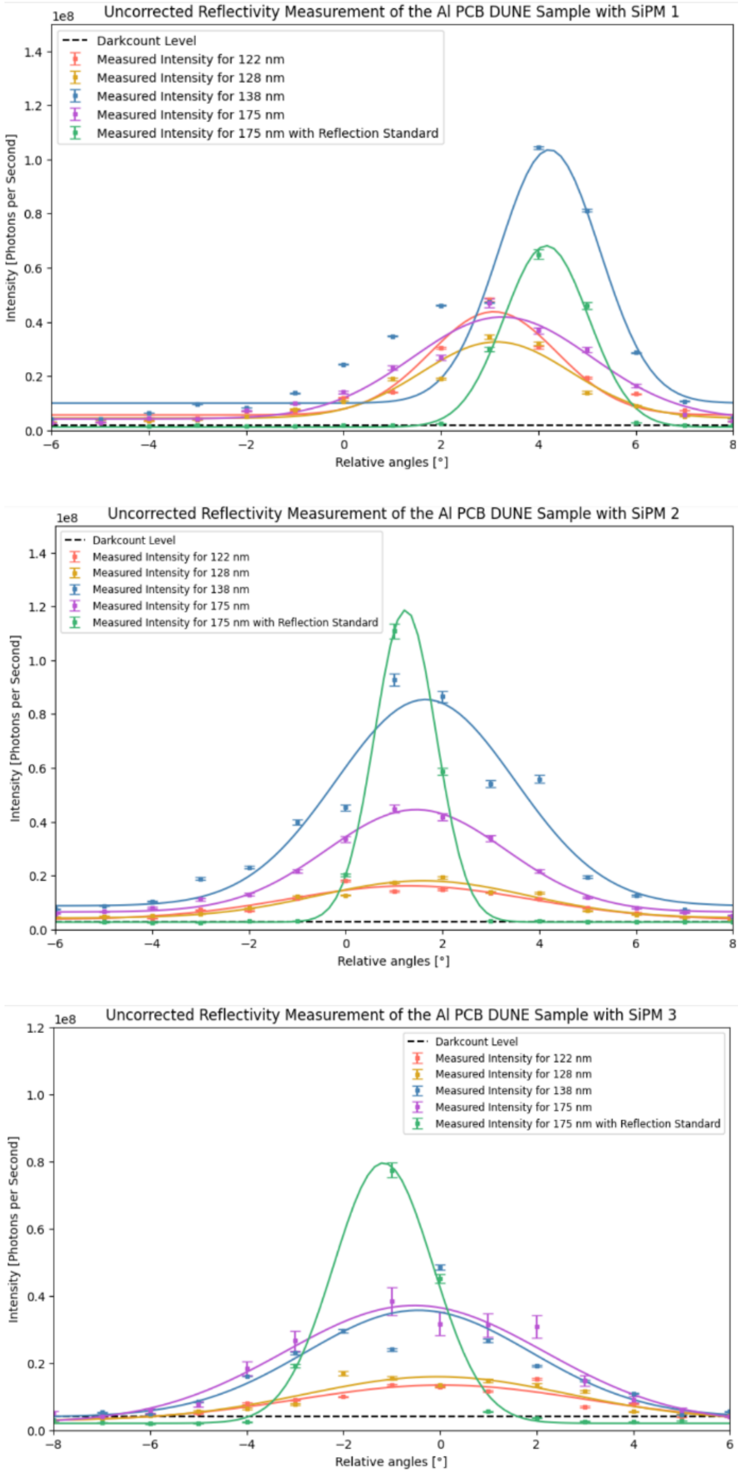

Figure 6.6: Uncorrected intensities of the light reflected by the Al PCB sample at the wavelengths of interest, and by the reflection standard at a reference wavelength of 175 nm. The error bars were propagated from the uncertainties described in Section 6.1.

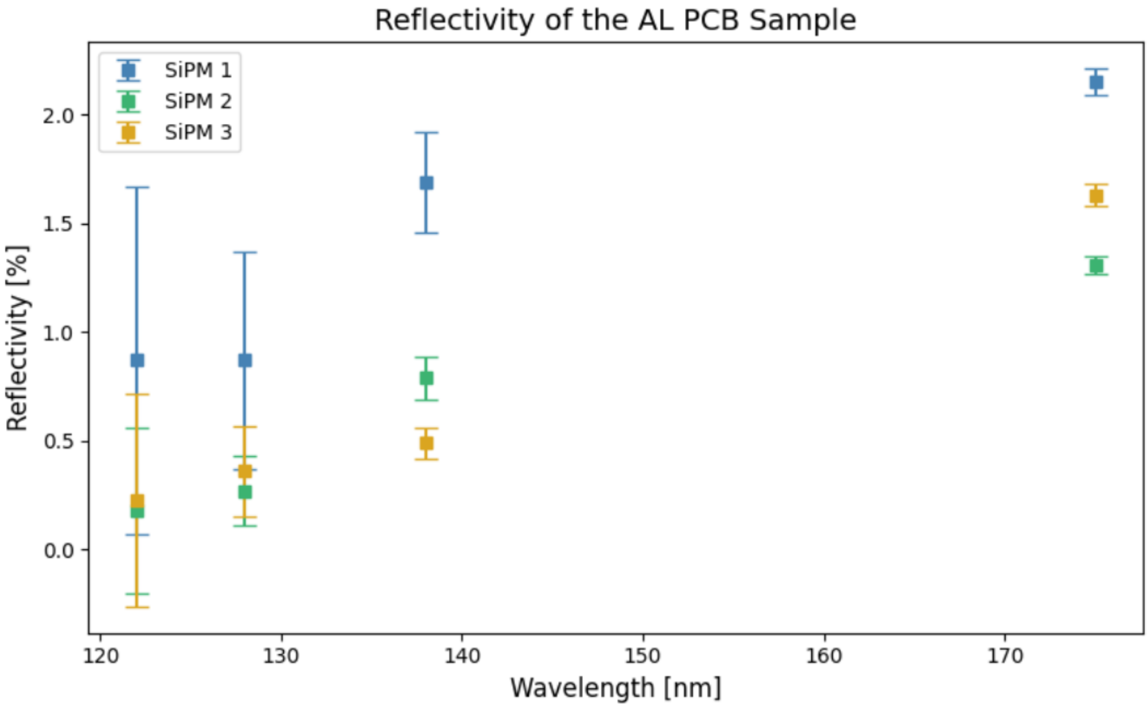

Figure 6.7: Calculated reflectivity of the Al PCB sample for the wavelengths of interest.

Al PCB Sample Reflectivity

Wavelength	SiPM 1	SiPM 2	SiPM 3
122 nm	$0.87 \pm 1.80\%$	$0.18 \pm 0.38\%$	$0.23 \pm 0.48\%$
128 nm	$0.87 \pm 0.50\%$	$0.27 \pm 0.16\%$	$0.36 \pm 0.21\%$
138 nm	$1.69 \pm 0.23\%$	$0.79 \pm 0.10\%$	$0.49 \pm 0.07\%$
175 nm	$2.15 \pm 0.06\%$	$1.31 \pm 0.04\%$	$1.63 \pm 0.05\%$

Table 6.2: Reflectivity of the Al PCB sample for the wavelengths of interest. The values are calculated using Equation 6.1 with the results presented in Figure 6.7.

6.2.1.2 Al Field Cage

The second sample for which the reflectivity is measured is an aluminum component from the field cage of the DUNE detector. The field cage plays an important role in generating the uniform electric field within the TPC. It makes up a large part of the detector's interior and thus understanding its optical properties is essential. A photograph of the aluminum field cage sample is shown in Figure 6.8. Figure 6.9 and Table 6.3 present the results of the calculated reflectivities. Figure 6.10 show the results of the intensity measurements performed to obtain these results.

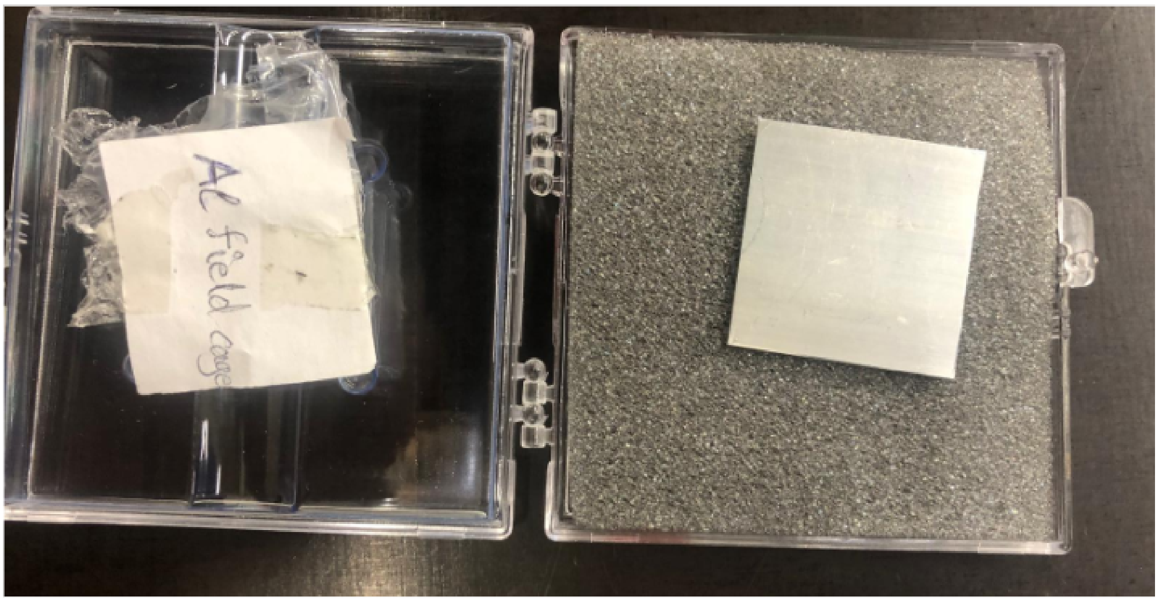

Figure 6.8: Photograph of the second DUNE sample from the aluminium field cage that is used for the reflectivity measurements.

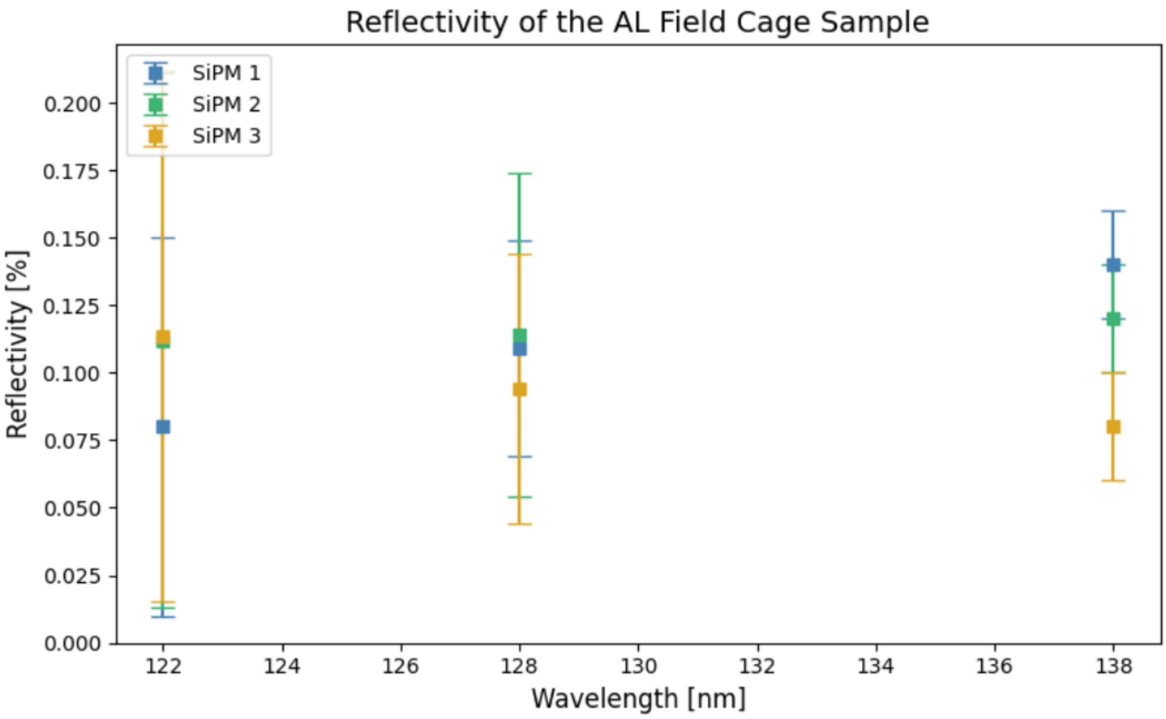

Figure 6.9: Calculated reflectivity of the Al Field Cage sample for the wavelengths of interest. The data or 175 nm was lost during a storage issue.

Al Field Cage Sample Reflectivity

Wavelength	SiPM 1	SiPM 2	SiPM 3
122 nm	$0.08 \pm 0.07\%$	$0.11 \pm 0.10\%$	$0.11 \pm 0.10\%$
128 nm	$0.11 \pm 0.04\%$	$0.11 \pm 0.06\%$	$0.09 \pm 0.05\%$
138 nm	$0.14 \pm 0.02\%$	$0.12 \pm 0.02\%$	$0.08 \pm 0.02\%$

Table 6.3: Reflectivity of the Al Field Cage sample from Figure 6.9. The values are calculated using Equation 6.1 with the results presented in Figure 6.10.

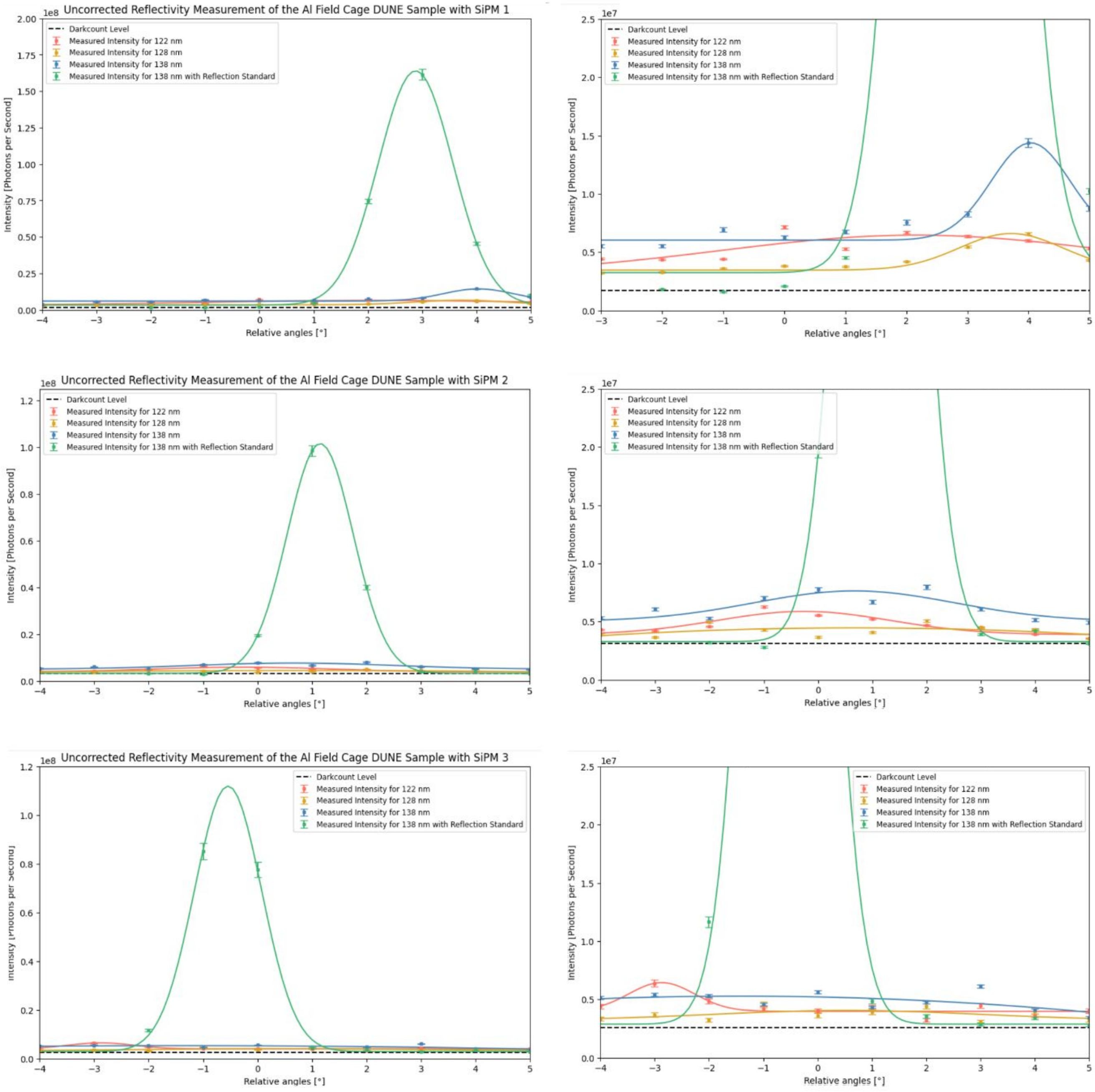

Figure 6.10: Uncorrected intensities of the light reflected by the Al Field Cage sample at the wavelengths of interest, and by the reflection standard at a reference wavelength of 138 nm. The error bars were propagated from the uncertainties described in Section 6.1. The results are presented from top two bottom for SiPM 1, 2 and 3. The figures on the left show the zoomed-in view of the figures on the right. These plots show that the peaks are not very pronounced, making the light intensity analysis difficult.

6.2.2 Conclusion and Discussion

The reflectivity of the DUNE samples at the LAr scintillation light wavelength of 128 nm was successfully measured. Overall, the results are satisfactory for a first reflectivity measurement at VULCAN. For the Al PCB sample, the measured reflectivities are $0.87 \pm 0.50\%$ for SiPM 1, $0.27 \pm 0.36\%$ for SiPM 2, and $0.36 \pm 0.21\%$ for SiPM 3. As shown in the intensity plots in Figure 6.6, the result for SiPM 1 deviates significantly from the results for SiPM 2 and 3. For SiPM 1, the measured intensity with the reflection standard is lower than the measured intensity with the sample at the same wavelength of 175 nm. This is notable because the sample and the reflection standard are both made of aluminum, with the standard being an undamaged, smooth mirror with UV-enhanced coating specifically designed to reflect light at lower wavelengths. Because the 175 standard measurement was used as a reference, the calculated reflectivities for SiPM 3 are higher. This is clearly visible in Figure 6.7. The discrepancy may be caused by the configuration of the vacuum sample chamber, where the angle of incidence of the light varies for each SiPM, with SiPM 3 being the most perpendicular to the incoming light beam and SiPM 1 the least. This raised concerns about combining the data from the three SiPMs, leading to the decision to present the results separately.

The measured reflectivity results for the Al Field Cage sample at 128 nm are $0.11 \pm 0.04\%$ for SiPM 1, $0.11 \pm 0.06\%$ for SiPM 2, and $0.09 \pm 0.05\%$ for SiPM 3. Analysis of the data presented in Figure 6.10 shows that this measurement captured very low levels of light. The light is also appears to be very diffused and the angle range does not cover the whole intensity peak. This makes it difficult to accurately fit the data and calculate the peak intensity. The low intensity of the reflected light may be partly attributed to the low reflectivity of the sample, but it was also caused by reduced intensity from the lamp. For the Al Field Cage sample measurement, a reference wavelength of 138 nm was used instead of 175 nm. At this wavelength the lamp intensity is very high, as shown in Figure 5.8. This high intensity led to saturation of the SiPM signal during measurements on the standard, which required slit sizes on the monochromator to be narrowed. For a repeat measurement it is recommended to select a reference wavelength that allows for a higher light intensity to measure the light reflected by the sample, without causing SiPM saturation for the measurement on the standard.

6.3 Limitations and Future Recommendations

To improve the accuracy and reliability of reflectivity and light measurements in the VUV setup at VULCAN, several considerations and recommendations are proposed for future experiments. A potential source of inaccuracies in this experiment is the correction factors that are used in the calibration of the reflection standard. These wavelength-dependent factors originating from the deuterium lamp, monochromator, and SiPM, are provided by the manufacturers without uncertainties. The accuracy of these calculated factors remains unknown. For more precise future measurements the values must be confirmed. It might be necessary to verify the lamp spectrum, monochromator reflectivity, and SiPM sensitivity through independent measurements.

In this experiment, the light intensity was measured based on the peak intensity that was observed during optimal alignment of the reflected light. To confirm that this accurately represents the true light intensity at that angle, the spot size of the light beam has to be established. If the reflected light covers multiple SiPMs, the contribution of the light on each SiPM and the dead regions between them should be taken into account. This was not adressed in this experiment because the spot size was estimated to fall within the boundaries of one SiPM. This estimation was not precise and should be redone for future light measurements. An alternative approach to avoid this issue is to use SiPMs with a larger active area. The calculation of light overlap on multiple SiPMs will also be necessary when considering diffusive reflection, which has also not been addressed in this experiment.

Further improvements can also be made to the design of the setup. The vacuum sample chamber does not allow for precise alignment and angle calculation of the sample holder and sensor holder. The angle of incidence on the sample affects the reflectivity as described in Equation 2.9. The reflectivity values provided by Hamamatsu for the reflection standard at 220 and 230 nm are based on an incidence angle of 45°. Since we cannot accurately measure the angle of our sample holder, we cannot correct for it. Additionally, by rotating the sample holder the angle of incidence on the stationary SiPMs varies a lot. Especially since the sensor holder is already at an unknown angle. This causes a discrepancy in the results of the three SiPMs which is discussed in Section 6.2.2. A possible solution is to make an adjustment to the current sensor holder that allows it to rotate with the orientation of the reflected beam, or to design an arm that rotates around the sample to capture the light while keeping the sample holder stationary.

To increase the accuracy of the measurements, a more reliable reflection standard should be used. The current standard lacks uncertainties and is not very precise at lower wavelengths according to the manufacturer. By using a standard with well-known reflectivity at wavelengths in the VUV range, a more accurate measurement calibration could be done. When the standard provides reflectivity data for wavelengths in the 100 - 200 nm range, the standard calibration would be unnecessary which reduces potential errors.

A final enhancement involves reducing the dark count rate. The dark count rate introduces noise that increases exponentially with temperature. This noise becomes more significant at low light levels. By cooling the SiPMs the dark count rate can be reduced. This can be done via the liquid nitrogen trap that is already installed on the vacuum chamber. The temperature sensor in the setup is currently floating in the vacuum. This sensor should be mounted to the SiPMs for accurate measurements of the dark count-temperature dependency.

References

[1] F. Close. *Neutrino*. OUP Oxford, 2010. 1, 3

[2] Pierre Ramond. **Neutrinos: A Glimpse beyond the standard model**. *Nucl. Phys. B Proc. Suppl.*, **77**:3–9, 1999. 1

[3] Bima Abi, R. Acciarri, Mario Acero, G. Adamov, Dianna Adams, M. Adinolfi, Z. Ahmad, Jawaira Ahmed, T. Alion, Saúl Alonso Monsalve, C. Alt, J. Anderson, Costas Andreopoulos, M. Andrews, M. Andriamirado, F. Andrianala, S. Andringa, A. Ankowski, J. Anthony, and R. Zwaska. **Deep Underground Neutrino Experiment (DUNE), Far Detector Technical Design Report, Volume 1 Introduction to DUNE**, 02 2020. 1, 6, 9

[4] Vittorio Boccone. **The ArDM project: A liquid argon TPC for dark matter detection**. *Journal of Physics: Conference Series*, **65**, 01 2007. 2, 8

[5] Peter W. Higgs. **Broken Symmetries and the Masses of Gauge Bosons**. *Phys. Rev. Lett.*, **13**:508–509, Oct 1964. 3

[6] F. Englert and R. Brout. **Broken Symmetry and the Mass of Gauge Vector Mesons**. *Phys. Rev. Lett.*, **13**:321–323, Aug 1964. 3

[7] CMS Collaboration. **A portrait of the Higgs boson by the CMS experiment ten years after the discovery**. *Nature*, **607**(7917):60–68, July 2022. 3

[8] W. Pauli. **Dear radioactive ladies and gentlemen**. *Phys. Today*, **31N9**:27, 1978. 3

[9] Fred Wilson. **Fermi's Theory of Beta Decay**. *American Journal of Physics*, **36**:1150, 12 1968. 4

[10] Susanne Mertens. **Direct Neutrino Mass Experiments**. *Journal of Physics: Conference Series*, **718**:022013, May 2016. 4

[11] X. Qian and P. Vogel. **Neutrino mass hierarchy**. *Progress in Particle and Nuclear Physics*, **83**:1–30, 2015. 4, 5

[12] Kate Scholberg. **Supernova Neutrino Detection**. *Annual Review of Nuclear and Particle Science*, **62**(1):81–103, November 2012. 5

[13] Roman Berner, Yifan Chen, Antonio Ereditato, Patrick P. Koller, Igor Kreslo, David Lorca, Thomas Mettler, Ting Miao, Francesco Piastra, James R. Sinclair, and Michael S. Weber. **First Operation of a Resistive Shell Liquid Argon Time Projection Chamber: A New Approach to Electric-Field Shaping**. *Instruments*, **3**(2), 2019. 6

[14] S Gao. **Cold Readout Electronics for Liquid Argon TPCs in the DUNE experiment**. *Journal of Physics: Conference Series*, **2374**:012075, 11 2022. 6

[15] Alexander Friedland and Shirley Weishi Li. **Understanding the energy resolution of liquid argon neutrino detectors**. *Physical Review D*, **99**(3), February 2019. 7

[16] Tadayoshi Doke, Kimiaki Masuda, and Eido Shibamura. **Estimation of absolute photon yields in liquid argon and xenon for relativistic (1 MeV) electrons**. *Nuclear Instruments and Methods in Physics Research Section A: Accelerators, Spectrometers, Detectors and Associated Equipment*, **291**(3):617–620, 1990. 8

[17] W. M. Bonivento and F. Terranova. **The science and technology of liquid argon detectors**, 2024. 8, 9

[18] C. Zhang and D.-M. Mei. **Evaluation of cosmogenic production of 39Ar and 42Ar for rare-event physics using underground argon**. *Astroparticle Physics*, **142**:102733, 2022. 8

[19] D. Gallacher, A. Leonhardt, H. Benmansour, E. Ellingwood, Q. Hars, M. Kuźniak, J. Anstey, B. Bondzior, M.G. Boulay, B. Cai, P.J. Dereń, P.C.F. Di Stefano, S. Garg, J. Mason, T.R. Pollmann, P. Skensved, V. Strickland, and M. Stringer. **Development and characterization of**

a slow wavelength shifting coating for background rejection in liquid argon detectors. *Nuclear Instruments and Methods in Physics Research Section A: Accelerators, Spectrometers, Detectors and Associated Equipment*, **1034**:166683, 2022. 9

[20] DUNE Collaboration, R. Acciarri, Mario Acero, Mark Adamowski, C. Adams, P. Adamson, Sourav Adhikari, Z. Ahmad, C. Albright, T. Alion, Eric Amador, J. Anderson, K. Anderson, Costas Andreopoulos, M. Andrews, Riana Andrews, Ionut Anghel, J.C Anjos, A. Ankowski, and Robert Zwaska. **Long-Baseline Neutrino Facility (LBNF) and Deep Underground Neutrino Experiment (DUNE) Conceptual Design Report Volume 2: The Physics Program for DUNE at LBNF**. 12 2015. 9

[21] Tommy Ohlsson. **Proton decay**. *Nuclear Physics B*, **993**:116268, 2023. 10

[22] FermiLab. **Deep Underground Neutrino Experiment**. `https://vms.fnal.gov/asset/detail?recid=1960180`, 2019. Accessed: 2024-10-05. 10

[23] Chetna Krishna. **ProtoDUNE's argon filling underway**. `https://home.cern/news/news/experiments/protodunes-argon-filling-underway`, 2024. Accessed: 2024-05-03. 10, 11

[24] William Emery and Adriano Camps. **Chapter 2 - Basic Electromagnetic Concepts and Applications to Optical Sensors**. In William Emery and Adriano Camps, editors, *Introduction to Satellite Remote Sensing*, pages 43–83. Elsevier, 2017. 12

[25] Stefan Gundacker and Arjan Heering. **The silicon photomultiplier: Fundamentals and applications of a modern solid-state photon detector**. *Physics in Medicine and Biology*, **65**, 08 2020. 13, 14

[26] Hamamatsu Photonics K.K. *VUV-MPPC 4th generation (VUV4)*. 13, 40, 45

[27] Fabio Acerbi and Stefan Gundacker. **Understanding and simulating SiPMs**. *Nuclear Instruments and Methods in Physics Research Section A: Accelerators, Spectrometers, Detectors and Associated Equipment*, **926**:16–35, 2019. Silicon Photomultipliers: Technology, Characterisation and Applications. 14

[28] Slawomir S. Piatek. **What is an SiPM and how does it work?**, 2016. `https://hub.hamamatsu.com/us/en/technical-notes/mppc-sipms/what-is-an-SiPM-and-how-does-it-work.html`. 15

[29] Jie Zheng, Zhuang Mao Png, Shi Hoe Ng, Guo Xiong Tham, Enyi Ye, Shermin S. Goh, Xian Jun Loh, and Zibiao Li. **Vitrimers: Current research trends and their emerging applications**. *Materials Today*, **51**:586–625, 2021. 16

[30] Alessandro Minotti and the DUNE collaboration. **Characterization of the DUNE photodetectors and study of the event burst phenomenon**. *Journal of Physics: Conference Series*, **2156**(1):012242, dec 2021. 16

[31] Y. Sun and J. Maricic. **SiPMs characterization and selection for the DUNE far detector photon detection system**. *Journal of Instrumentation*, **11**(01):C01078–C01078, January 2016. 16

[32] C. C. W. van de Post. *Building a sample chamber for measuring the reflectivity and transparency of detector materials at VUV wavelengths*. Master's thesis, TU Delft, 2022. `https://wiki.nikhef.nl/vuv/Main_Page`. 18, 20, 21, 25

[33] Hamamatsu Photonics K.K. *ELECTROSTATIC CHARGE REMOVERS*, 2023. 22, 47

[34] Hamamatsu Photonics K.K. *DEUTERIUM LAMPS (D2 LAMPS)*, 2021. 22

[35] Jasmijn Stevens. **Lamp Spectrum Measurement**, 2022. `https://wiki.nikhef.nl/vuv/Lamp_spectrum_measurement`. 22

[36] McPherson Inc. *234/302 200mm f.l. Vacuum Monochromator*. 22, 24, 47

[37] Pfeiffer Vacuum. *Operating Instruction HiCube 80 ECO*. 24, 46

[38] L. Wang, M.Y. Guan, H.J. Qin, C. Guo, X.L. Sun, C.G. Yang, Q. Zhao, J.C. Liu, P. Zhang, Y.P. Zhang, W.X. Xiong, Y.T. Wei, Y.Y. Gan, and J.J. Li. **Characterization of VUV4 SiPM for liquid argon detector**. *Journal of Instrumentation*, **16**(07):P07021, July 2021. 27

[39] Stefan Seifert, Herman T. van Dam, Jan Huizenga, Ruud Vinke, Peter Dendooven, Herbert Lohner, and Dennis R. Schaart. **Simulation of Silicon Photomultiplier Signals**. *IEEE Transactions on Nuclear Science*, **56**(6):3726–3733, 2009. 30

[40] Lucia. **Dark count dependence on temperature**, 2023. `https://wiki.nikhef.nl/vuv/Dark_count_dependence_on_temperature`. 51

[41] Olaf Stenzel, Steffen Wilbrandt, Jian-Ying He, Sven Stempfhuber, Sven Schröder, and Andreas Tünnermann. **A Model Surface for Calculating the Reflectance of Smooth and Rough Aluminum Layers in the Vacuum Ultraviolet Spectral Range**. *Coatings*, **13**:122, 01 2023. 56, 57

[42] Alessandra Martucci, Alberta Aversa, and Mariangela Lombardi. **Ongoing Challenges of Laser-Based Powder Bed Fusion Processing of Al Alloys and Potential Solutions from the Literature—A Review**. *Materials*, **16**:1084, 01 2023. 56

[43] Derrick Langley, Ronald Coutu, Jr, Lavern Starman, and Stanley Rogers. **Optical metamaterials for photonics applications**. *Proceedings of SPIE - The International Society for Optical Engineering*, 08 2009. 56

[44] Taehoon Kim, Gwangmook Kim, Hyeohn Kim, Hong-Jib Yoon, Taeseong Kim, Yohan Jun, Tae-Hyun Shin, Shinill Kang, Dosik Hwang, Byungwook Min, and Wooyoung Shim. **Megahertz-wave-transmitting conducting polymer electrode for device-to-device integration**. *Nature Communications*, **10**:653, 02 2019. 56